



On the onset of runaway stellar collisions in dense star clusters – II. Hydrodynamics of three-body interactions

Evgenii Gaburov,^{1,2,3*} James C. Lombardi Jr.⁴ and Simon Portegies Zwart^{1,2,3}

¹Leiden Observatory, Leiden Observatory, Leiden, the Netherlands

²Astronomical Institute ‘Anton Pannekoek’, University of Amsterdam, Amsterdam, the Netherlands

³Section Computational Science, University of Amsterdam, Amsterdam, the Netherlands

⁴Department of Physics, Allegheny College, Meadville, PA 16355, USA

Accepted 2009 October 18. Received 2009 October 18; in original form 2009 April 6

ABSTRACT

The onset of runaway stellar collisions in young star clusters is more likely to initiate with an encounter between a binary and a third star than between two single stars. Using the initial conditions of such three-star encounters from direct N -body simulations, we model the resulting interaction by means of smoothed particle hydrodynamics (SPH). Our code implements new equations of motion that allow for efficient use of non-equal mass particles and is capable of evolving contact binaries for thousands of orbits, if not indefinitely. We find that, in the majority of the cases considered, all three stars merge together. In addition, we compare our SPH calculations against those of the sticky-sphere approximation. If one is not concerned with mass loss, then the sticky sphere approach gives the correct qualitative outcome in approximately 75 per cent of the cases considered. Among those cases in which the sticky-sphere algorithm identifies only two particular stars to collide, the hydrodynamic calculations find the same qualitative outcome in about half of the instances. If the sticky-sphere approach determines that all three stars merge, then the hydrodynamic simulations invariably agree. However, in such three-star mergers, the hydrodynamic simulations reveal that: (i) mass lost as ejecta can be a considerable fraction of the total mass in the system (up to ~ 25 per cent); (ii) due to asymmetric mass loss, the collision product can sometimes receive a kick velocity that exceeds 10 km s^{-1} , large enough to allow the collision product to escape the core of the cluster; and (iii) the energy of the ejected matter can be large enough (up to $\sim 3 \times 10^{50} \text{ erg}$) to remove or disturb the inter cluster gas appreciably.

Key words: gravitation – hydrodynamics – methods: numerical – binaries: general.

1 INTRODUCTION

Stars are born in clusters, which upon formation are generally dense and massive. In recent years, it has become clear that clusters remain bound even after losing a considerable fraction of their mass due to primordial out-gassing (Baumgardt & Kroupa 2007). The subsequent dynamical evolution of these clusters leads to a state of core collapse (Portegies Zwart et al. 2007b), almost irrespective of the number of primordial binaries (Portegies Zwart et al. 2004); primordial binaries do, however, appear to delay the collapse of the core (Fregeau et al. 2003; Heggie, Trenti & Hut 2006). In addition, clusters with appropriate initial conditions may form a very massive star by means of runaway stellar collisions (Portegies Zwart et al. 2004). Such an object has been hypothesized to be a progenitor

of an intermediate mass black hole (however, see Glebbeek et al. 2009).

Even if binaries are not present at the birth of a star cluster, they can form via three-body encounters during the process of core collapse. Indeed, the expansion of the cluster core after deep gravothermal collapse (Sugimoto & Bettwieser 1983) is mediated by binaries, regardless of the presence or absence of a primordial population. During post-core collapse evolution, a cluster may enter a phase of gravothermal oscillations (Cohn, Hut & Wise 1989), allowing periods of high interaction rate and providing further opportunity for binaries and single stars to interact closely.

Analytic expressions describing encounters between a binary and a third star, all treated as point masses, have been derived for various portions of parameter space (Heggie 1975; Hut 1983; Heggie & Hut 1993). In addition, complementary numerical surveys have been performed in the point mass approximation by a number of authors (Harrington 1970; Hut & Bahcall 1983; Hills 1992).

*E-mail: egaburov@strw.leidenuniv.nl

During triple encounters, however, individual stars may approach close enough to each other that the approximation of point-particle dynamics breaks down: the size and internal structure of the stars then play a major role in determining the outcome of the encounter. Consequently, some numerical studies have augmented the point-mass treatment with simplified models that incorporate several hydrodynamic effects (McMillan 1986; Fregeau et al. 2004). Large-scale N -body simulations of clusters have demonstrated the ubiquity of resonance interactions in dynamically unstable triples (Portegies Zwart et al. 1999) – the scenarios that ultimately may lead to the coalescence of all three stars (Fregeau et al. 2004). The accurate modelling of the details under which triples merge, and whether or not two or all three stars in an encounter participate in the merger, has a profound consequence for the occurrence of collision runaways (Portegies Zwart & McMillan 2002; Freitag, Gürkan & Rasio 2006) and whether or not such runaways can lead to the formation of binaries among intermediate mass black holes (Gürkan, Fregeau & Rasio 2006).

The first three-dimensional hydrodynamic calculations of encounters between a binary and a single star were performed by Cleary & Monaghan (1990) with the smoothed particle hydrodynamics (SPH) method. However, computational constraints at that time limited their work to a very small number of SPH particles (usually 136 per star) and to $n = 1.5$ polytropes, appropriate only for white dwarfs or extremely low-mass main-sequence stars. Subsequent hydrodynamic treatments of three-body interactions typically confined themselves to scenarios in which at least one of the stars was a compact object and therefore could be treated as a point mass (e.g. Davies, Benz & Hills 1993a, 1994). Davies et al. (1998) and Adams, Davies & Sills (2004) consider three-body encounters between a binary and a red giant star as a mechanism for destroying red giants near the centres of dense stellar systems. Their hydrodynamic simulations follow the fluid of the red giant envelope during the encounter, with the red giant core and both components of the binary being treated as point masses. Because only the red giant envelope is treated hydrodynamically, the only mergers that can result are those which form a binary of the two-point masses surrounded by an envelope donated from the red giant.

Numerous hydrodynamic simulations of colliding stars have studied the structure of the merger product (Benz & Hills 1987; Davies, Benz & Hills 1994; Lombardi, Rasio & Shapiro 1995; Davies et al. 1998; Lombardi et al. 2002; Freitag & Benz 2005; Dale & Davies 2006; Gaburov, Lombardi & Portegies Zwart 2008b). In some cases the subsequent stellar evolution of collision products is followed (Suzuki et al. 2007; Glebbeek et al. 2009), especially within the context of the formation and evolution of blue stragglers (Sills et al. 2001; Sills, Adams & Davies 2005; Glebbeek & Pols 2008; Glebbeek, Pols & Hurley 2008; Sills, Karakas & Lattanzio 2009). Such collision studies, however, have been focused on encounters between two single stars, ignoring for the time being that collisional cross-sections and rates can be large for systems consisting of three or more stars.

The scenario of triple-star mergers among low-mass main-sequence stars has been previously considered by Lombardi et al. (2003) using SPH. Their calculations indicate that the collision product always has a significantly enhanced cross-section and that the distribution of most chemical elements within the final product is not sensitive to many details of the initial conditions. They, however, concentrated solely on low-mass stars and treated the triple star merger as two separate, consecutive parabolic collisions.

Recently, Gaburov, Gualandris & Portegies Zwart (2008a) performed an extensive and detailed study to investigate the circumstances under which a first collision between stars occurs. Using direct N -body integration with sticky spheres of realistic stellar sizes, they argued that binaries tend to catalyse collisions. In their simulations, the binaries that are formed during core collapse tend to interact with an incoming star, which subsequently merges with one of the binary components. The results of Lombardi et al. (2003) suggest that the hydrodynamics of such interactions are unlikely to keep the binary itself undamaged. Instead, it is quite likely that the stellar material that is expelled during a collision engulfs the system in a common envelope, leading to the merger of all three stars.

In this paper, we introduce a new implementation of SPH and apply it to follow accurately the hydrodynamics of encounters between hard binaries and intruders. We concentrate on cases involving massive main-sequence stars, such as those found in young star clusters, treating all three stars simultaneously and with realistic orbital parameters determined from a dynamical cluster calculation. In particular, the initial conditions are selected from the set of N -body simulations carried out by Gaburov et al. (2008a), but with the internal structure of the stars now being determined by a stellar evolution code. A comprehensive survey of triple-star collisions would need to explore an enormous amount of parameter space, but here we focus on a number of representative cases. In total, we selected 40 encounters from the simulations of Gaburov et al. (2008a). Among these are random selections, as well as some that are specifically chosen because of their relevance for the subsequent N -body evolution or because of their uncertain outcome given the relatively simple treatment of mergers in the N -body simulations.

This paper is structured as follows. In Section 2 and Appendix A, we introduce our new formulation of SPH, which allows efficient use of non-equal mass particles, as well as our approach for relaxing single stars. In Section 3, we describe how we model close and contact binary star systems, and we demonstrate the stability of these systems for at least the time interval of interest. The set of initial conditions for the three-body collisions are presented in Section 4 and Appendix B. Finally, Section 5 presents, while Section 6 discusses, the results of our calculations.

2 METHODS AND CONVENTIONS

2.1 SPH code

SPH is the most widely used hydrodynamics scheme in the astrophysics community. It is a Lagrangian particle method, meaning that the fluid is represented by a finite number of fluid elements or ‘particles’. Associated with each particle i are, for example, its position \mathbf{r}_i , velocity \mathbf{v}_i , specific internal energy u_i , and mass m_i . Each particle also carries a purely numerical smoothing length h_i that determines the local spatial resolution and is used in the calculation of fluid properties such as acceleration and density (see Monaghan 1992, Rasio & Lombardi 1999 and Rosswog 2009 for reviews of SPH).

Although our code evolves from the one presented in Lombardi et al. (2006), we have significantly modified the dynamical equations to allow for efficient use of non-equal mass particles. This enhancement, along with the current artificial viscosity and time-stepping algorithms, is presented in Appendix A. So that we can model main-sequence stars of any mass, we include both ideal gas and radiation pressure in the equation of state, in the way described by Lombardi et al. (2006).

2.2 Determination of bound and ejecta components

In the post-processing of our simulations, we wish to calculate the time evolution of the positions and masses of gravitationally bound components, the mass in a circumbinary envelope, and the mass in ejecta. To determine such quantities, we implement an iterative procedure that generalizes the method of Lombardi et al. (2006) to up to three stars. As a minimal requirement to be considered part of a gravitationally bound component, an SPH particle essentially must have a negative total energy with respect to the centre of mass of that component. More specifically, for a particle i to be part of stellar component j of mass M_j , the quantity $v_{ij}^2/2 + u_i - GM_j/\max(d_{ij}, h_i)$ must be negative, where v_{ij} is the velocity of particle i with respect to the centre of mass of component j and d_{ij} is the distance from particle i to that centre of mass. If this condition holds for more than one component j , then the particle is assigned to the component that has a centre of mass closest to particle i .

Once the algorithm has converged, so that it is known which particles are associated with which components, we calculate the centre of mass position and velocity of each component. If there are two bound components, we then compute the eccentricity e of their orbit and consider them a binary if $e < 1$. If there are three bound components, we compute the eccentricity and semimajor axis a of all pairs of components. If one of those pairs has an eccentricity $e < 1$, then we consider it a binary; if more than one pair has $e < 1$, then we consider only the pair with the smallest apastron separation $a(1 + e)$ to be a binary. A particle that is not assigned to a bound component can either be part of the ejecta or, if a binary exists, a circumbinary envelope. A particle is associated with the circumbinary envelope if it has a negative total energy when measured relative to the centre of mass of the binary.

2.3 Choice of units

Throughout this paper, numerical results are given in units where $G = M_\odot = R_\odot = 1$, where G is the Newtonian gravitational constant and M_\odot and R_\odot are the mass and radius of the Sun. The units of time, velocity and energy are then

$$t_u = \left(\frac{R_\odot^3}{GM_\odot} \right)^{1/2} = 1594 \text{ s}, \quad (1)$$

$$v_u = \left(\frac{GM_\odot}{R_\odot} \right)^{1/2} = 437 \text{ km s}^{-1}, \quad (2)$$

$$E_u = \frac{GM_\odot^2}{R_\odot} = 3.79 \times 10^{48} \text{ erg}. \quad (3)$$

2.4 Relaxing a single star

Before initiating a triple star collision, we must first prepare an SPH model for each star in isolation. To compute the structure and composition profiles of our parent stars, we use the TWIN stellar evolution code (Eggleton 1971; Glebbeek & Pols 2008; Glebbeek 2008) from the MUSE software environment (Portegies Zwart, McMillan & Harfst 2009).¹ We evolve main-sequence stars with initial helium abundance $Y = 0.28$ and metallicity $Z = 0.02$ for a time $t = 2 \text{ Myr}$,

¹ <http://muse.li>

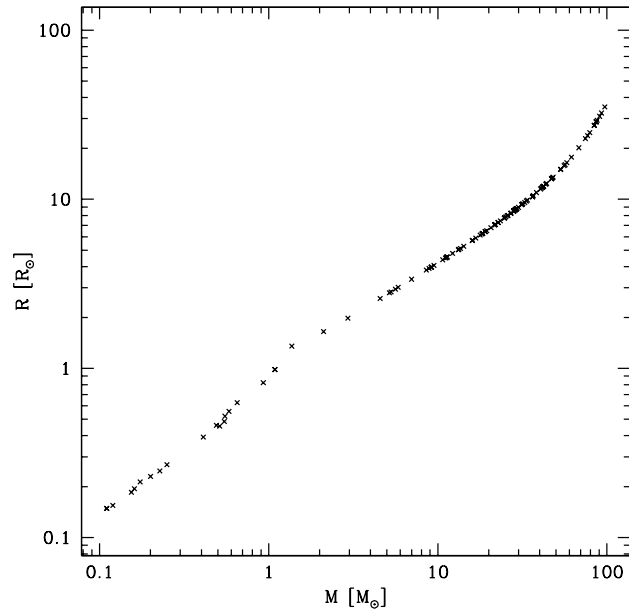


Figure 1. Stellar radius versus mass at 2 Myr, as given by the TWIN stellar evolution code, for the stars considered in this paper.

a small enough age that even the most massive stars in a star cluster are still on the main sequence. The mass-radius relation which results from these calculations is shown in Fig. 1.

Initially, we place the SPH particles on a hexagonal close packed lattice, with particles extending out to a distance only a few smoothing lengths less than the full stellar radius. After the initial particle

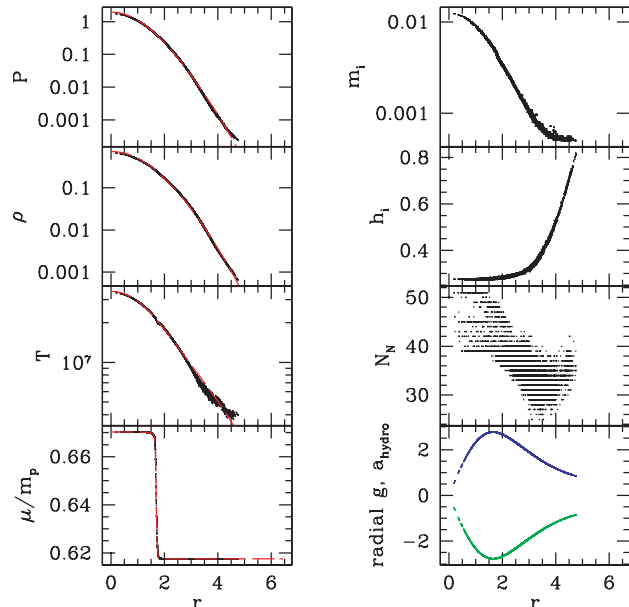


Figure 2. Properties of the SPH model for a $19.1 M_\odot$ star. Profiles are shown as a function of radius, after relaxation for 730 time units. The frames in the left-hand column show profiles of pressure P , density ρ , temperature T (in Kelvin) and mean molecular weight μ in units of the proton mass m_p , with the dashed curve representing results the TWIN evolution code and dots representing particle data from our SPH model. The right-hand column provides additional SPH particle data: individual SPH particle mass m_i , smoothing length h_i , number of neighbours N_N and radial component of the hydrodynamic acceleration a_{hydro} (upper data) and gravitational acceleration g (lower data).

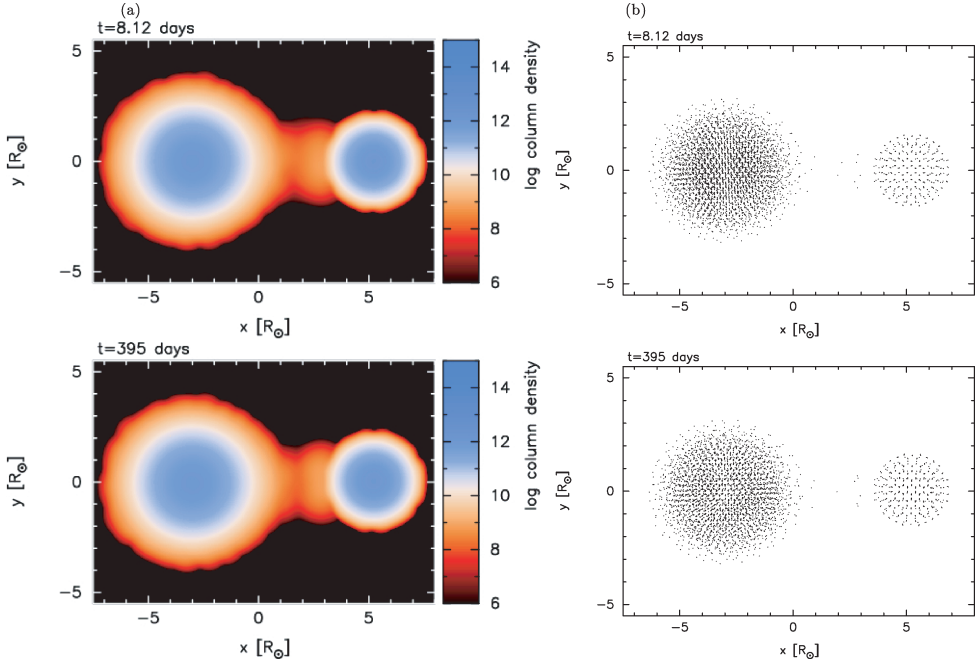


Figure 3. A contact binary consisting of a $12.2 M_{\odot}$ primary and a $6.99 M_{\odot}$ secondary both at the end of the relaxation (upper frames) and after dynamical evolution through more than 600 orbits (lower frames). (a) In the left-hand column, colours represent column density, measured in g cm^{-2} on a log base 10 scale, along lines of sight perpendicular to the orbital plane. (b) In the right-hand column, we show projections of particle positions on to the orbital plane.

parameters have been assigned according to the desired profiles from TWIN, we allow the SPH fluid to evolve into hydrostatic equilibrium. During this calculation, we include the artificial viscosity contribution to the SPH acceleration equation so that energy is conserved, and we do not include a drag force on the particles. For the relaxation calculations of massive stars ($M \gtrsim 30 M_{\odot}$), we do, however, implement a method to keep low-mass particles from being pushed to large radii: namely, during the initial stages of the relaxation, we implement a variation on the XSPH method (Monaghan 1992, 2002), in which the velocity used to update positions is the average of the actual particle velocity and the desired particle velocity (zero). In practice, this method is trivial to implement: one simply divides the particle velocity by two before updating positions. All our relaxed models remain static and stable when left to dynamically evolve in isolation.

This approach allows us to model the parent stars very accurately. We present an example in Fig. 2, where we plot desired profiles and SPH particle data for a $19.1 M_{\odot}$ star. The structure and composition profiles of the SPH model closely follow those from TWIN profiles, and the model remains stable when evolved dynamically.

We note that our new SPH equations of motion help suppress spurious particle noise and allow the use of fewer neighbours than in traditional SPH schemes, which usually require at least approximately 30 neighbours per particle. In the model represented in Fig. 2, for example, the neighbour number N_N falls as low as 25, with 279 out of the 7692 particles having fewer than 30 neighbours. By keeping the neighbour number small, we achieve a better spatial resolution without increasing total particle number. We provide further justification of our choice in Appendix A.

3 PREPARING A BINARY

In this section, we present our algorithm to model the close binary systems that are used in most of the triple star collisions (see

Section 5). The first step in creating a binary is to relax each of the two stellar components in isolation, as described in the previous section. In the case of detached binaries, we place these relaxed stellar models along the x -axis with their centres of mass separated by the desired separation r . For contact binaries, however, we begin with the stars well separated and gradually decrease the semimajor

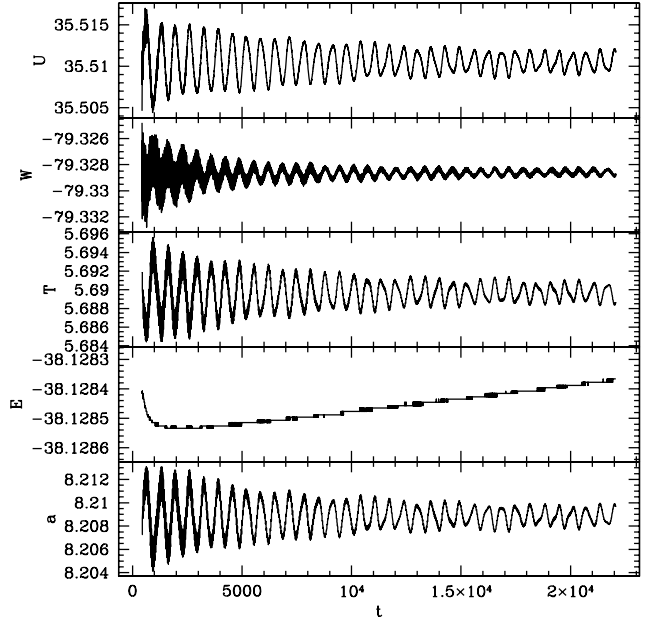


Figure 4. Internal energy U , gravitational potential energy W , kinetic energy T , total energy E and semimajor axis a versus time t for the dynamical evolution of the contact binary shown in Fig. 3. The time interval shown spans more than 600 orbits. The orbital period is 35 time units, while the epicyclic period is 650 time units.

axis until the desired separation is achieved, in order to minimize oscillations initiated by tidal forces. In all cases, the centre of mass of the system remains fixed in space, which we choose to be the origin.

During the binary the relaxation process, the positions of the particles within each star are adjusted at each time-step by simple uniform translations along the binary axis until the separation between the centres of mass reaches the desired separation r . Simultaneously, the angular velocity Ω_{orb} defining the corotating frame is continuously updated, such that the net centrifugal and gravitational accelerations of the two stars cancel exactly:

$$\Omega_{\text{orb}}^2 = -\frac{1}{2} \left(\frac{\sum_{*1} m_i \dot{v}_{x,i}}{\sum_{*1} m_i x_i} + \frac{\sum_{*2} m_i \dot{v}_{x,i}}{\sum_{*2} m_i x_i} \right), \quad (4)$$

where \sum_{*j} symbolizes a sum over all particles in star j . Here, the Cartesian coordinate x is measured along the binary semimajor axis; $\dot{v}_{x,i}$ is the acceleration of particle i parallel to the axis of the binary in an inertial frame. A centrifugal acceleration is given to all particles such that the system approaches a steady state corresponding to a synchronized binary. As in the relaxation process of a single star, we also include the artificial viscosity contribution to the SPH acceleration equation.

This approach allows us to create close binaries that remain in dynamically stable orbits for many hundreds of orbits, if not indefinitely. An example is presented in Figs 3 and 4. In Fig. 3, we plot (a) column densities and (b) particle positions for a contact binary both before and after dynamical evolution through over 600 orbits. In this particular case, there are 4908 particles in the $12.2 M_{\odot}$ star

and 510 in the 6.99 solar mass star. Seven particles, each of mass $6 \times 10^{-4} M_{\odot}$ and having originated from the primary, remain stably in the vicinity of the inner Lagrangian point between the stars throughout the dynamical evolution: see frame (b) of Fig. 3. While this particular simulation is not high enough resolution to resolve fully the extremely low-density bridge between the stars, it does highlight the ability of our code to keep even low-mass particles in stable equilibria during long dynamical evolution calculations.

In Fig. 4, we show time evolution of various energies for the same binary. The epicyclic oscillations, with a period of 650 time units, are clearly visible. The fact that the epicyclic period is more than an order of magnitude larger than the orbital period of 35 time units underscores how close this binary is to the dynamical stability limit. As a binary approaches this limit, the epicyclic period would formally approach infinity (Rasio & Shapiro 1994). The innermost dynamically stable orbit then marks the transition when the squared frequency of the epicyclic oscillations passes from a positive to a negative value, so that the qualitative behaviour of perturbations changes from oscillatory to exponential. Throughout the calculation, the perturbations remain small and actually damp with time: the internal energy U remains constant to within about 0.03 per cent, the gravitational energy W to within about 0.008 per cent and the kinetic energy to within about 0.2 per cent. Meanwhile, the total energy is conserved within about 0.0004 per cent.

In another example, we relaxed a contact binary with a 92.9 , and a $53.3 M_{\odot}$ star with semimajor axis of $43.8 R_{\odot}$. In Fig. 5, we show snapshots for every 50 time units (0.92 d) of the binary during and after the relaxation process.

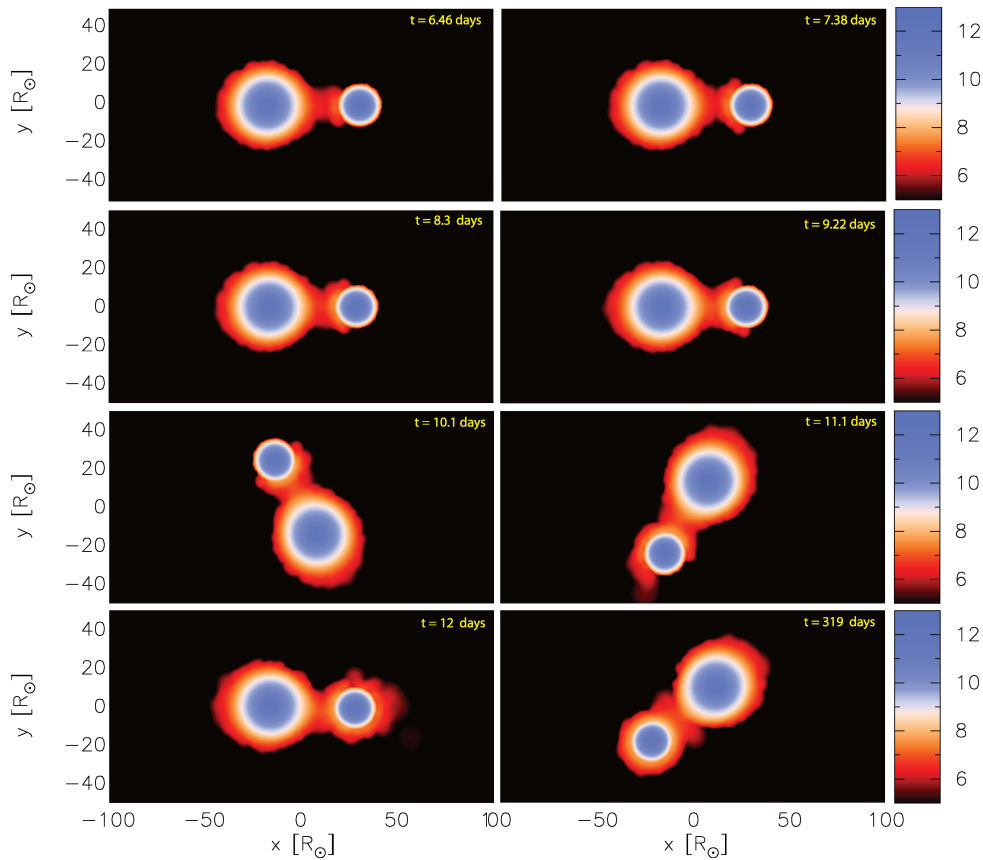


Figure 5. The relaxation and dynamical evolution of a close binary between 92.9 and $53.3 M_{\odot}$ with the semimajor axis equal to $43.8 R_{\odot}$. The orbital period of the binary is 2.78 d (150.6 time units). The calculation switches from a corotating frame to an inertial frame at a time of 9.22 d. As in Fig. 3, colours represent column density on a logscale in units of g cm^{-3} .

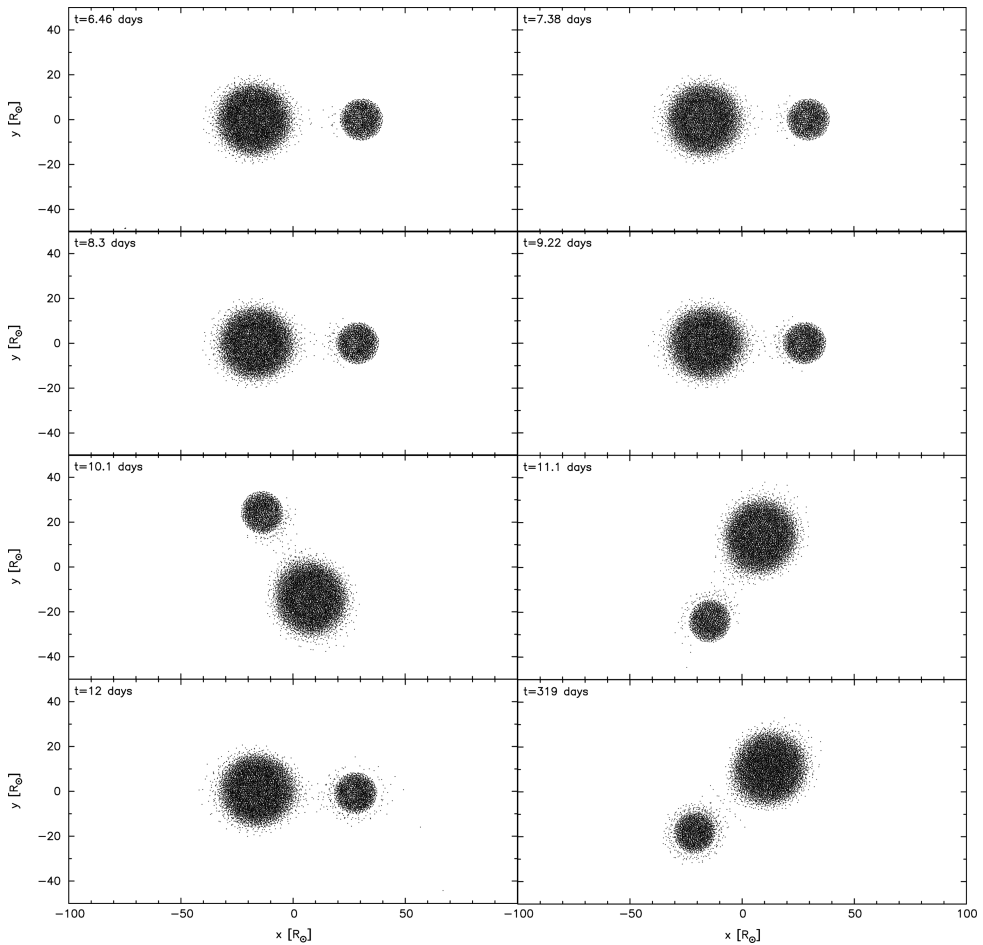


Figure 6. Particle plot of the Fig. 5.

We begin with an initial semimajor axis of $55.8 R_{\odot}$, and we decrease it to $43.8 R_{\odot}$ in 500 time units (9.2 d). The topmost left-hand panel shows the binary during relaxation at a time of 350 units (6.5 d), and the semimajor axis at this time is equal to $48.0 R_{\odot}$. It is possible to note commencement of mass transfer from the primary on to the secondary. At the time of 500 units (9.22 d), when the semimajor axis becomes $43.8 R_{\odot}$, we stop the relaxation and dynamically evolve the system in the inertial frame. At this time half of the secondary star is already submerged in the fluid of the primary star. By the time of 650 units (12 d), the secondary star is completely engulfed in the fluid of the primary star. This behaviour is natural because the entropy in the outer layers of the $92.2 M_{\odot}$ star is higher than that of the $53.3 M_{\odot}$ star. For hydrodynamical stability, the fluid with high entropy should be on top of the fluid with the lower entropy, and this is exactly what occurs in the simulation. This effect in stellar collisions is known as entropy sorting (Lombardi et al. 2002; Gaburov et al. 2008b).

The bottommost right-hand panel shows a binary at the time of 17 300 units (319 d), and the semimajor axis maintains its value of $43.8 R_{\odot}$. In Fig. 7, we show energy and semimajor axis of the binary as a function of time.

4 INITIAL CONDITIONS

The parameter space of three-body encounters is immense, leaving no hope to be completely covered with SPH simulations. The

approach we take here is to study part of it by using the initial conditions obtained from direct N -body simulation. In particular, we take initial conditions for three-body collisions from Gaburov et al. (2008a) who carried out an extensive set of N -body simulations of young star clusters. In these simulations, the stars were modelled as hard spheres with a given mass and corresponding radius. A collision occurs when two spheres experience physical contact, or in other words, when the separation between the centre of these spheres is equal to the sum of their radii. This treatment of collisions, known as the sticky sphere approximation, conserves total mass and momentum.

In this paper, however, we resolve the stellar structure and focus on isolated close three-body interactions. This can be justified since usually such interactions last less than a year, and therefore local conditions hardly change on such a short time-scale. We split all three-body interactions into two groups: the interaction between a binary and a single star, and the interaction between three single stars which are in the middle of a resonant interaction. The latter case is straightforward to model, as we need to prepare only relaxed single star models, as described in Section 2, and then assign the appropriate initial positions and velocities to each of the stars. The actual dynamical interaction process is then modelled using the SPH code.

In the case of an interaction between a binary and a single star, we initially relax the binary as described in Section 3. The binary separation is taken from the N -body simulations. Because most of the

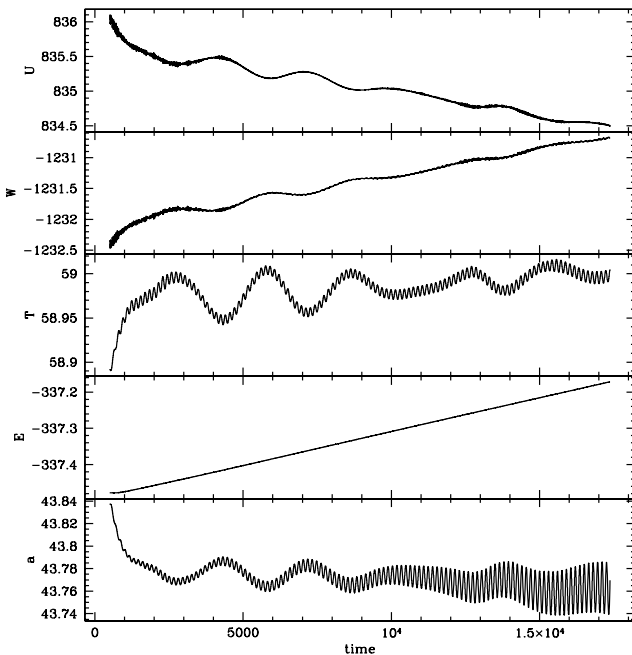


Figure 7. Internal energy U , gravitational potential energy W , kinetic energy T , total energy E and semimajor axis a versus time t for the dynamical evolution of an isolated close binary consisting of a $92.9 M_{\odot}$ primary and a $53.3 M_{\odot}$ secondary star. All quantities remain within 0.2 per cent of their initial value throughout the simulation of more than 100 orbits, highlighting the ability of our code to evolve stably even those binaries in deep contact. The small increase in the total energy occurs due to a few low-mass particles that are escaping to infinity.

binaries have separations of a few stellar radii, tidal circularization plays an important role, and therefore eccentricity of these binaries is nearly equal to zero. In some of the cases, the synthetic stellar evolution part of N -body calculations predicts a binary separation too small to be dynamically stable, and in such cases we relax an SPH model of the binary near the smallest possible semimajor axis such that the binary remains stable or quasi-stable, such that the merger time-scale is at least a few thousand time units.

Table 1 lists the initial positions and trajectories for the binary-single encounters in a way that is meant to aid the mental visualization of each case: for example, comparing the periastron separation $r_{\text{p,ib}}$ to the binary semimajor axis a_{12} provides an indication of where the intruder strikes within the binary. The ratio $E_{\text{ib}}/|E_{12}|$ gives a measure of how much energy is being brought to the system by the intruder, relative to the binding energy of the binary. A negative value of $E_{\text{ib}}/|E_{12}|$ implies that the intruder star is bound to the binary, otherwise it is initially unbound. We note, however, that the magnitude of this ratio is much less than unity, which corresponds to a nearly parabolic encounter between the intruder and the binary star. Indeed, in almost all of these cases the trajectory of the intruder about the binary is nearly parabolic ($0.9 < e < 1.1$). The last column indicates the angle of approach of the intruder towards the binary, with $0 \leq \theta \leq 180^\circ$. More precisely, the angle θ is the angle between the angular momentum vector \mathbf{L}_{12} of the binary and the angular momentum vector \mathbf{L}_3 of the intruder calculated about the centre of mass of the binary (Fig. 8). For example, $\theta = 0$ corresponds to coplanar trajectories with the intruder orbiting the binary in the same direction (clockwise or counter-clockwise) as the binary is orbiting; $\theta = 90^\circ$ corresponds to the third star incident on the binary from a direction perpendicular to the orbital plane of

Table 1. In the first column, we present the case identification number. The second and third columns show the masses of the binary components, while the fourth column gives the mass of the intruder. The fifth column gives the semimajor axis a_{12} of the binary. Columns 6 and 7 gives the periastron separation $r_{\text{p,ib}}$ and eccentricity e_{ib} , respectively, of the equivalent two-body Kepler orbit between the intruder and the centre of mass of the binary. Column 8 gives the ratio of the energy E_{ib} in this orbit of the intruder and binary to the binding energy $|E_{12}|$ of the binary itself. Column 9 gives the angle θ , in degrees, between the angular momentum of the binary and the angular momentum of the intruder about the binary (see Fig. 8).

ID	$m_{\text{b},1}$	$m_{\text{b},2}$ (M_{\odot})	m_i	a_{12}	$r_{\text{p,ib}}$ (R_{\odot})	$E_{\text{ib}}/ E_{12} $	θ ($^\circ$)
203	47.1	36.3	1.09	33.8	33.3	-7.6e-3	80
206	24.6	21.9	20.6	13.3	7.46	+1.7e-1	68
207	42.2	18.2	0.65	30.6	16.3	+3.0e-1	124
208	86.7	0.16	0.51	54.0	6.27	+3.8e-2	41
211	61.7	8.89	18.4	23.3	52.8	+1.1e-1	42
212	87.6	27.1	22.7	35.1	10.9	-7.0e-2	102
213	76.8	13.6	0.23	32.3	2.77	+2.2e-3	160
217	86.4	28.9	0.11	51.1	9.58	+1.2e-3	123
222	22.8	11.1	5.28	34.8	10.5	+3.4e-1	73
223	28.6	4.57	19.4	13.0	12.1	-4.3e-3	107
224	48.1	22.0	0.2	22.5	5.85	+2.6e-3	147
227	16.0	0.17	5.62	25.6	4.05	-1.2e-1	59
231	25.8	0.411	26.1	26.0	12.9	-4.4e-1	43
232	12.2	6.99	19.1	8.26	2.10	+1.7e-4	20
233	28.9	2.94	47.6	26.7	12.2	+1.0e-2	91
236	40.5	31.4	29.3	23.5	19.2	+1.4e-2	84
241	28.1	11.3	41.7	13.6	12.8	-1.6e-2	51
242	41.1	23.5	0.490	21.3	1.54	-2.5e-3	142
245	43.5	16.0	79.1	33.2	32.7	-2.0e-2	97
246	42.2	38.3	1.37	28.4	19.1	+8.7e-3	161
249	74.7	0.11	0.15	101	5.88	-1.6e-1	51
250	44.0	31.9	0.550	36.4	3.48	-2.1e-1	63
253	53.4	8.55	0.583	22.4	12.5	-2.5e-2	35
256	33.4	2.11	5.84	18.6	7.50	-5.2e-2	58
257	97.3	24.9	5.18	51.5	2.69	-2.9e-1	132
258	90.4	0.55	0.93	28.6	10.2	-3.5e-3	86
259	55.9	21.7	11.4	26.3	6.72	+2.9e-2	46
260	92.9	53.3	13.3	43.9	54.6	+5.7e-1	14
267	28.6	14.2	19.1	26.3	0.28	-5.3e-1	126
298	56.7	25.3	28.1	26.2	18.9	-1.8e-1	143
299	52.3	16.9	52.3	26.2	0.0	-0.952e-4	94

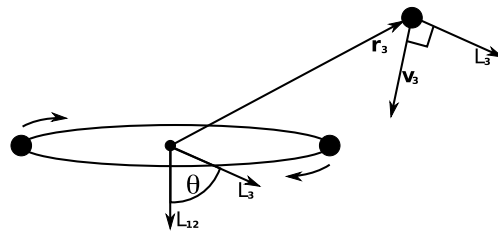


Figure 8. The orientation of a binary and an intruder star.

the binary; and $\theta = 180^\circ$ again corresponds to coplanar trajectories, although now the intruder approaches with an angular momentum that is antiparallel to that of the binary. All of our initial binaries are on nearly circular orbits ($e_{12} < 0.02$), with the exception of case 249 ($e_{12} = 0.41$).

We initiate two types of hydrodynamic calculations. The first type, which comprises the majority of our calculations, consists of a corotating binary intruded upon by a third star. In these situations, a circular binary is relaxed as we described in Section 3. If it is a

Table 2. The masses, in solar masses, of single stars which participate in the resonance interaction.

ID	m_1	m_2 (M_\odot)	m_3
201	84.1	0.25	27.1
202	57.9	0.12	29.9
204	42.4	11.5	16.5
214	9.49	16.8	17.8
219	36.6	9.10	10.7
220	84.3	68.3	32.7
257	5.18	24.9	97.3
261	33.9	13.2	9.17
262	29.3	31.5	18.4

Note. The first column shows the case number, while the following columns give the masses of participating stars.

contact binary, then the circular orbit is maintained, with the orbital plane and phase being shifted to match those of the desired initial conditions. If the binary is detached, then the velocity of each star is adjusted to give not only the desired orbital orientation and phase, but the eccentricity as well. In this way, we account for rotation and tidal bulging in the binary components. The third star, relaxed as described in Section 2, is initially not rotating and separated from the binary by many times the radius of the larger star, which allows us to neglect its tidal effects in the initial configuration.

The second type of hydrodynamic calculation involves the collision of three individual stars (Table 2). These also represent cases in which a binary is disrupted by an intruder. In these cases, the three stars are caught in a long-lived resonant interaction that would be too computationally expensive to follow entirely with the hydrodynamic code. Each of the three stars is first relaxed by the means described in Section 2. Their initial positions and velocities in the collision calculation represent a snapshot from the point-mass dynamical calculation in which the stars were widely separated but nearing the end of their resonant interaction.

In Appendix B, we present the raw initial conditions of our calculations in order to facilitate comparisons with any future works.

5 RESULTS

In this section, we report on the results of 40 simulations of different encounters between three stars. In terms of computational time, most of the runs are performed with $N \sim 10^4$ and lasted somewhere between 1 and 2 weeks on a modern PC. The self-gravity was computed by direct summation on a special purpose MD-GRAPE3 hardware (Fukushige et al. 1996) or an NVIDIA graphics cards (Hamada & Iitaka 2007; Portegies Zwart, Belleman & Geldof 2007a; Belleman, Bédorf & Portegies Zwart 2008; Gaburov, Harfst & Portegies Zwart 2009). The code employs a shared time-step algorithm, and the total number of integration steps is usually between 10^5 and 10^6 . The longest run was simulated until $t \sim 10^5 t_{\text{dyn}}$ in about 10^6 time-steps, which results in an average time-step of $\sim 0.1 t_{\text{dyn}}$. Our higher resolution calculations ($N \sim 10^5$) typically require a few months to complete.

5.1 Selected cases

In Table 3, we summarize the outcomes of all collisions from Tables 1 and 2. Binaries are represented by (1, 2) while resonances are represented by (1, 2, 3), with the masses satisfying $M_1 > M_2 > M_3$.

The merger product between stars 1 and 2, due either to a binary coalescence or a direct collision, is represented using braces, $\{1, 2\}$, where the more massive component at the time of the merger is listed first. In addition, the notation can be embedded. Consider, for example, case 242 with the following interaction sequence: (1,2),3 → (1,2,3) → $\{\{1,3\},2\} \rightarrow \{2,\{1,3\}\}$. The initial state (1,2),3 represents a primary 1 and a secondary 2 in a binary being intruded upon by the least massive star 3. The (1,2,3) indicates that there is neither an immediate retreat of the intruder nor an immediate merger, but instead the three stars move in a resonance interaction. The state $\{\{1,3\},2\}$ means that the intruder has merged with the primary, leaving the merger product in a binary with the secondary star. Finally, $\{2,\{1,3\}\}$ indicates that these two remaining objects coalesce. Note that in this final state, the secondary star indicated to the left of $\{1,3\}$ within the outer braces, because the former was more massive at the time of the merger due to dynamical mass transfer during the final stages of binary inspiral.

Here, we present several cases in greater detail. First, in Figs 9 and 10, we show trajectories and column density plots, respectively, from calculations of case 232, in which a $12.2 + 6.99 M_\odot$ binary collides with a $19.1 M_\odot$ intruder. The setup of the initial conditions for these three particular stars is described in Section 2 (Figs 2–4). Fig. 10(a) shows the three bodies shortly after the start of the calculation. Fig. 10(b) shows the three bodies just prior to the impact and merger of the intruder and the secondary from the binary. The first apocentre passage in the resulting binary star is shown in Fig. 10(c), while Fig. 10(d) shows the binary in the process of merger. In Fig. 10(e), we show the snapshot shortly after the fluid from the three stars has merged into a single object, and finally, Fig. 10(f) shows a snapshot from near the end of our calculation: the merger product has drifted away from the origin due to asymmetric mass loss. In this case, the merger product has little angular momentum, and the calculated mass loss quickly asymptotes to a constant value of approximately $2.6 M_\odot$ (see Fig. 11).

As another example, we consider case 260 in which a massive binary (92.9 and $53.3 M_\odot$) is perturbed by a less massive intruder ($13.3 M_\odot$). Here, the intruder is a catalyst that triggers binary merger. In Fig. 12, we show time evolution of energies (left-hand panel) and global quantities (right-hand panel), such as the masses of individual stars and ejected fluid. In Fig. 13, we present time snapshots for this run. Fig. 13(a) shows a snapshot at the beginning of the simulations, and Fig. 13(b) at the moment of closest approach between the intruder star and the binary. The binary merger process is shown in Figs 13(c)–(e). It can be seen that the fluid is gradually lost from the L2 Lagrangian point. Finally, the merged binary is shown in Fig. 13(f). In contrast to case 232, binary orbital angular momentum is converted into spin of the product, explaining the elongated shape of the collision product in Fig. 13(f). One may also note that the collision product is quickly drifting away from the centre with a velocity of 14 km s^{-1} . Most of this kick velocity comes from the escaping intruder star rather than from the asymmetric mass ejection.

The second episode of mass ejection, which occurs after the binary merger as can be seen in the right-hand panel of Fig. 12, is an artefact of the artificial viscosity used in SPH. Initially, the collision product is in a state of both differential rotation and hydrostatic equilibrium. Artificial viscosity tends to transfer angular momentum from the rapidly rotating shells to slower ones (Lombardi et al. 1999), and this forces the product towards rigid body rotation. Since the inner regions of the collision product are spinning much faster than the outer ones, the angular momentum is transferred outwards. The net effect is that the inner regions of the collision product

Table 3. Summary of the 40 simulations for three-star interactions.

ID	Method	Outcome	Speed (km s ⁻¹)	f_L	E_{ej} (10 ⁴⁸ erg)
201	pm	(1,2,3) → (1,2),3	0.8, 352		
	ss	(1,2,3) → ({1,3},2)	0		
14 118		(1,2,3) → ({1,3},2)	<0.1	<0.001	<0.1
28 296		(1,2,3) → ({1,3},2)	<0.1	<0.001	<0.1
113 046		(1,2,3) → ({1,3},2)	<0.1	<0.001	<0.1
202	pm	(1,2,3) → (1,2),3	0.7, 529		
	ss	(1,2,3) → ({1,3},2)	0		
6138		(1,2,3) → ({1,3},2)	<0.1	<0.001	<0.1
11 466		(1,2,3) → ({1,3},2)	<0.1	<0.001	<0.1
22 380		(1,2,3) → ({1,3},2)	<0.1	<0.001	<0.1
91 956		(1,2,3) → ({1,3},2)	<0.1	<0.001	<0.1
203	pm	(1,2),3 → (1,2,3) → (1,2),3	6.24, 480		
	ss	(1,2),3 → (1,2,3) → ({1,3},2)	0		
10 398		(1,2),3 → (1,2,3) → ({1,3},2)	<0.1	<0.001	0.13
204	pm	(1,2,3) → (1,3), 2	40.6, 143		
	ss	(1,2,3) → ({1,3},2) → {2,{1,3}}	0		
11 946		(1,2,3) → ({1,2},{3}) → {{1,2},3}	7.2	0.13	12.
60 024		(1,2,3) → ({1,2},3) → {{1,2},3}	3.8	0.082	12.
206	pm	(1,2),3 → (1,2,3) → (1,2),3	60.7, 136		
	ss	(1,2),3 → (1,{2,3}) → {{2,3},1}	0		
14 475		(1,2),3 → (1,2,3) → ({1,2},3) → {{1,2},3}	1.2	0.048	13.
207	pm	(1,2),3	3.31, 308		
	ss	(1,2),3 → (1,{2,3})	0		
9492		(1,2),3	3.7, 345	0	0
208	pm	(1,3),2	1.02, 555		
	ss	(1,3),2 → ({1,2},3)	0		
15 018		(1,3),2 → ({1,2},3)	<0.1	<0.001	0.22
211	pm	(1,3),2	91.4, 824		
	ss	(1,3),2 → {1,3},2	53.1, 203		
11 028		(1,3),2 → {1,3},2	39, 146	0.026	6.7
212	pm	(1,2),3 → (1,2,3) → (1,3),2	34.3, 139		
	ss	(1,2),3 → ({1,3},2) → {{1,3},2}	0		
22 080		(1,2),3 → (1,2,3) → ({1,3},2) → {{1,3},2}	3.6	0.17	66.
213	pm	(1,2),3	1.82, 724		
	ss	(1,2),3 → ({1,3},2)	0		
13 314		(1,2),3 → ({1,3},2)	<0.1	<0.001	<0.1
125 130		(1,2),3 → ({1,3},2)	<0.1	<0.001	1.5
214	pm	(1,2,3) → (1,2),3	95, 348		
	ss	(1,2,3) → ({1,2},3)	0		
11 016		(1,2,3) → ({2,1},3) → {{2,1},3}	1.4	0.14	3.9
217	pm	(1,2),3 → (1,2,3) → (1,2),3	0.7, 713		
	ss	(1,2),3 → ({1,3},2)	0		
17 442		(1,2),3 → ({1,3},2)	<0.1	<0.001	<0.1
139 656		(1,2),3 → ({1,3},2)	<0.1	<0.001	<0.1
219	pm	(1,2,3) → (1,2),3	49, 255		
	ss	(1,2,3) → ({1,3},2) → {{1,3},2}	0		
14 160		(1,2,3) → ({1,2},3) → {{1,2},3}	8.1	0.038	33.
220	pm	(1,2,3) → (1,2),3	166, 778		
	ss	(1,2,3) → ({1,2},3) → {{1,2},3}	0		
20 178		(1,2,3) → (1,{2,3}) → {{2,3},1}	14.	0.062	130
46 296		(1,2,3) → (1,{2,3}) → {{2,3},1}	11.	0.062	130
222	pm	(1,2),3	38.3, 246		
	ss	(1,2),3 → ({1,3},2) → {{1,3},2}	0		
17 076		(1,2),3	48, 310	0	0
223	pm	(1,3),2 → (1,2,3) → (1,2),3	43, 454		
	ss	(1,3),2 → ({1,2},3) → {{1,2},3}	0		
12 456		(1,3),2 → (1,2,3) → ({2,1},3) → {{2,1},3}	12.	0.25	14.

Table 3 – *continued*

ID	Method	Outcome	Speed (km s ⁻¹)	f_L	E_{ej} (10 ⁴⁸ erg)
224	pm	(1,2),3	0.858, 323		
	ss	(1,2),3 → {{1,3},2}	0		
14 472		(1,2),3 → (1,2,3) → {{1,3},2} → {{1,3},2}	0.94	0.023	3.4
227	pm	(1,3),2 → (1,2,3) → (1,3),2	19, 55		
	ss	(1,3),2 → {{1,2},3} → {{1,2},3}	0		
10 008		(1,3),2 → (1,2,3) → {{1,2},3} → {{1,2},3}	3.6	0.027	2.3
231	pm	(2,3),1 → (1,2,3) → (1,2),3	71, 72		
	ss	(2,3),1 → {{1,2},3}	1.3, 163		
13 554		(2,3),1 → (1,2,3) → {{1,3},2} → {2,{1,3}}	0.25	0.036	1.9
232	pm	(2,3),1 → (1,2,3) → (1,2),3	106, 107		
	ss	(2,3),1 → (1,{2,3}) → {{2,3},1}	0		
13 110		(2,3),1 → {{1,3},2} → {{1,3},2}	4.0	0.067	20.
233	pm	(2,3),1 → (1,3),2	18.7, 487		
	ss	(2,3),1 → {{1,2},3} → {{1,2},3}	0		
13 020		(2,3),1 → (1,2,3) → {{1,2},3} → {{1,2},3}	3.7	0.17	20
236	pm	(1,2),3 → (1,2,3) → (2,3),1	39, 58		
	ss	(1,2),3 → (1,{2,3}) → {{2,3},1}	0		
12 672		(1,2),3 → (1,2,3) → {{1,2},3} → {{1,2},3}	5.8	0.14	25.
241	pm	(2,3),1 → (1,2,3) → (1,3),2	68.1, 128		
	ss	(2,3),1 → {{1,3},2} → {{1,3},2}	0		
19 956		(2,3),1 → (1,2,3) → {{1,3},2} → {{1,3},2}	8.0	0.086	32.
242	pm	(1,2),3	6.5, 856		
	ss	(1,2),3 → {{1,3},2} → {{1,3},2}	0		
10 224		(1,2),3 → (1,2,3) → {{1,3},2} → {2,{1,3}}	0.26	0.016	2.0
245	pm	(2,3),1 → (1,2,3) → (1,2),3	31.2, 23.9		
	ss	(2,3),1 → {{1,3},2} → {{1,3},2}	0		
16 884		(2,3),1 → (1,2,3) → {{1,2},3} → {{1,2},3}	5.3	0.027	26.
246	pm	(1,2),3	3, 194		
	ss	(1,2),3 → (1,{2,3}) → {1,{2,3}}	0		
5232		(1,2),3 → (1,2,3) → {{1,3},2} → {2,{1,3}}	2.5	0.017	7.6
10 554		(1,2),3 → (1,2,3) → (1,2),3 → {{1,2},3}	11.8, 691	0.010	3.7
21 204		(1,2),3 → (1,2,3) → (1,{2,3}) → {{1,2,3}}	1.1	0.023	6.3
42 294		(1,2),3 → (1,2,3) → (1,{2,3}) → {{1,2,3}}	0.71	0.020	5.3
84 642		(1,2),3 → (1,2,3) → {{1,2},3} → {{1,2},3}	3.4	0.096	7.9
249	pm	(1,3),2 → (1,2,3) → (1,3),2	0.06, 30		
	ss	(1,3),2 → {{1,2},3}	0		
10 374		(1,3),2 → {{1,2},3}	<0.1	<0.001	<0.1
82 812		(1,3),2 → {{1,2},3}	<0.1	<0.001	<0.1
250	pm	(1,2),3 → (1,2,3) → (1,2),3	2.3, 324		
	ss	(1,2),3 → (1,2,3) → {{1,3},2}	0		
10 254		(1,2),3 → (1,2,3) → {{1,3},2}	0.4	<0.001	0.54
253	pm	(1,2),3	2.0, 212		
	ss	(1,2),3 → {{1,3},2}	0		
10 374		(1,2),3 → {{1,2},3}	1.0, 176	0.032	5.3
256	pm	(1,3),2 → (1,2,3) → (1,3),2	39, 234		
	ss	(1,3),2 → {{1,2},3} → {{1,2},3}	0		
10 200		(1,3),2 → (1,2,3) → {{1,2},3} → {{1,2},3}	7	0.15	11.
257	pm	(1,2,3) → (1,2),3	11, 257		
	ss	(1,2,3) → {{1,3},2} → {{1,3},2}	0		
10 236		(1,2,3) → {{1,3},2} → {{1,3},2}	2.9	0.087	36.
258	pm	(1,3),2	0.8, 79		
	ss	(1,3),2 → {{1,2},3} → {{1,2},3}	0		
10 104		(1,3),2 → (1,2,3) → {{1,2},3} → {{1,2},3}	0.6	<0.001	2.0
259	pm	(1,2),3	52, 353		
	ss	(1,2),3 → {{1,3},2} → {{1,3},2}	0		
10 272		(1,2),3 → (1,2,3) → {{1,3},2} → {{1,3},2}	5	0.085	30.

Table 3 – continued

ID	Method	Outcome	Speed (km s ⁻¹)	f_L	E_{ej} (10 ⁴⁸ erg)
260	pm	(1,2),3 → (1,2,3) → (1,2),3	31.0, 340		
	ss	(1,2),3 → (1,{2,3})	0		
22 518		(1,2),3 → {1,2},3	44, 456	0.024	6.6
261	pm	(1,2,3) → (1,2),3	39, 198		
	ss	(1,2,3) → ({1,3},2)	0		
10 092		(1,2,3) → ({1,3},2)	7.1	0.020	22.
262	pm	(1,2,3) → (1,2),3	69, 226		
	ss	(1,2,3) → (1,{2,3})	0		
10 314		(1,2,3) → (1,2),3 → {2,1},3	68, 223	0.011	2.1
267	pm	(1,3),2 → (1,2),3	403, 905		
	ss	(1,3),2 → ({1,3},2) → {2,{1,3}}	0		
14 934		(1,3),2 → ({1,2},3) → {{1,2},3}	9.6	0.063	67.
298	pm	(1,3),2 → (1,2,3) → (1,2),3	60, 200		
	ss	(1,3),2 → ({1,2},3) → {{1,2},3}	0		
13 818		(1,3),2 → (1,2,3) → ({1,3},2) → {{1,3},2}	7	0.21	52.
299	pm	(1,3),2 → (1,2,3) → (2,3),1	128, 797		
	ss	(1,3),2 → ({1,2},3) → {{1,2},3}	0		
10 194		(1,3),2 → ({1,2},3) → {{1,2},3}	6.9	0.15	310
102 540		(1,3),2 → ({1,2},3) → {{1,2},3}	2.7	0.16	330

Note. The first column gives the case identification number. The second column either gives the number N of SPH particles used to simulate this case, or names the treatment as ‘pm’ (point mass) or ‘ss’ (sticky spheres). The third column summarizes the interaction that resulted by listing all changes in the state of the system. The fourth column lists the projected speed(s) at infinity of the resulting object(s), in units of km s⁻¹. The fifth column gives the fractional mass loss 200 time units after the final change of state, while the sixth column lists the total energy ejected, in units of 10⁴⁸ erg, at that same time.

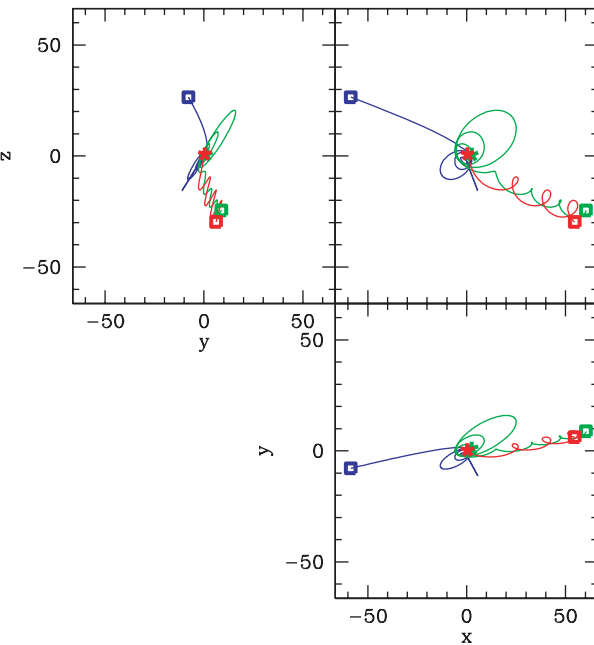


Figure 9. Trajectories in the xy (lower right), xz (upper right) and yz (upper left) planes for case 232, as given by our hydrodynamics calculation. The initial conditions are marked by squares, while the final position of an object before merger is marked by a 5-point asterisk.

contract, because of loss of the rotational support, but the outer regions expand because of the continuously increasing supply of angular momentum, and this case can be seen in Fig. 14. Eventually, these outer regions become unbound and escape, and this results in the second episode of the mass loss. The mass loss we

report in Table 1 is before this second episode but after the first, corresponding to the plateau $M_{ej} \approx 4 M_\odot$ near $t = 7500$ in Fig. 12.

From the data of Table 3, it is evident that when only two stars merge the mass loss remains below a few per cent, and often considerably smaller. It is known that mass loss in a parabolic collision between two main-sequence stars is small (Freitag & Benz 2005; Gaburov et al. 2008b). The mass-loss percentage is typically larger in cases where all three stars ultimately merge, exceeding 10 per cent in the hydrodynamic simulations of cases 212, 214, 223, 233, 236, 256, and 298. The hydrodynamic evolution in these more extreme cases is qualitatively similar: the first merger event is between the most massive star and one of the other two, and typically occurs after a short resonant interaction. The resulting merger product is enhanced in size by shock heating and rotation, leaving its outermost layers loosely bound. The third star, often after being flung out to a large distance, can experience several periastron passages through the envelope of the first merger product before ultimately donating its fluid to the mix. In the process, substantial amounts of gas are ejected from the diffuse envelope at every periastron passage.

An example of this type of interaction is summarized in Figs 15 and 16 for case 298, which involves a $56.7 M_\odot + 25.3 M_\odot$ binary being intruded upon by a $28.1 M_\odot$ star. The features of these curves can be associated with events during the encounter. In this situation, the intruder initiates a short-lived resonance that ends with the induced merger of the binary components near $t = 400$. As can be seen in the middle frame of Fig. 16, approximately $2 M_\odot$ of fluid is ejected in the process. The intruder retreats on an eccentric orbit, reaching an apastron separation of more than $200 R_\odot$ and returning for its next pericentre passage shortly before $t = 1000$. As the intruder moves through the outer layers of the first merger product, its orbit decays and more mass is ejected. By $t = 1400$,

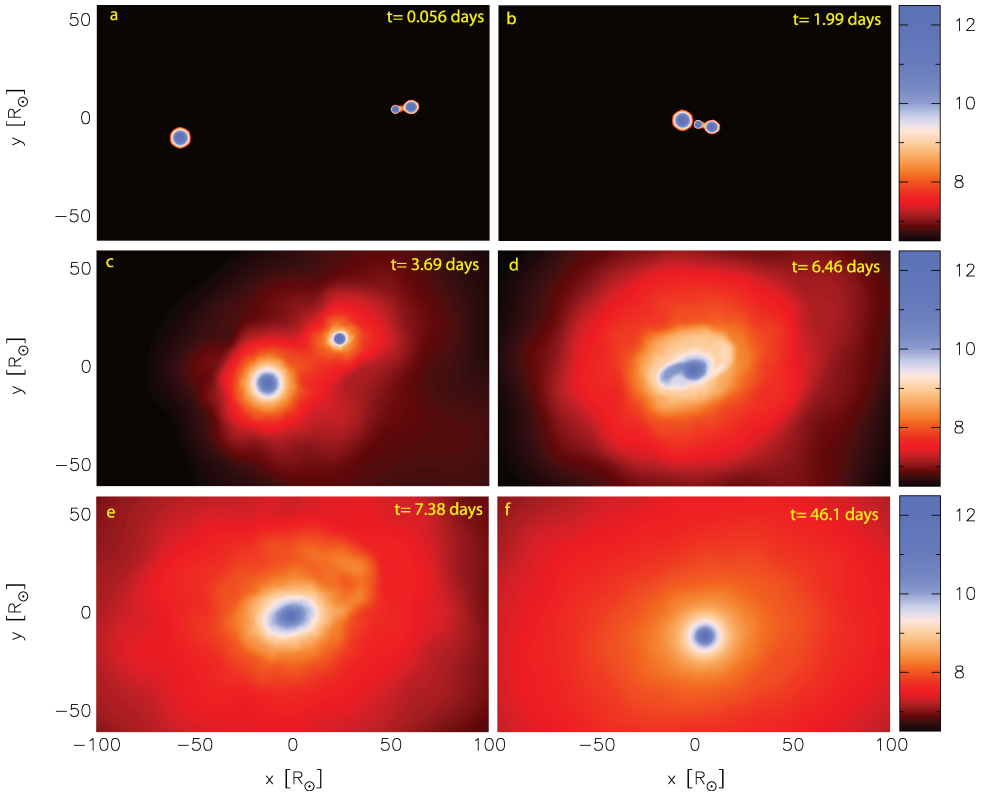


Figure 10. Column density along lines of sight perpendicular to the xy plane at various times for the same hydrodynamic calculation of case 232 presented in Fig. 9. As in previous figures, colours represent column density in units of g cm^{-2} on a logscale.

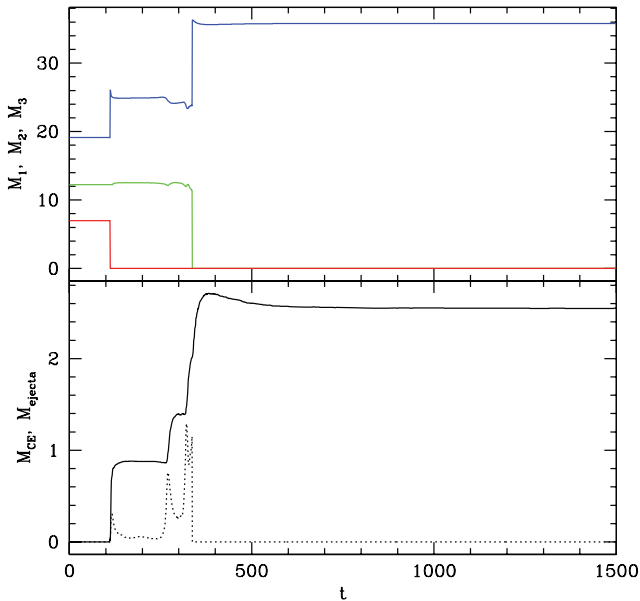


Figure 11. Masses versus time for case 232. The top frame shows the time evolution of the mass of the primary, secondary and intruder. The bottom frame shows the amount of mass ejected (solid curve) and bound in a circumbinary envelope (dotted curve).

the three-body merger product is formed and more than $20 M_{\odot}$ has been ejected in total.

Another double merger resulting in significant mass loss is summarized in Fig. 17, which shows the masses and separations relevant

to the hydrodynamic calculation of case 256 (a $33.4 + 2.11 M_{\odot}$ binary and a $5.84 M_{\odot}$ intruder). Here, the initial merger occurs between the two most massive stars near $t = 1800$, with about $1.5 M_{\odot}$ of fluid is ejected in the process. The third star is left on a highly eccentric orbit, reaching an apastron separation of more than $600 R_{\odot}$ at $t = 4100$, and returning for its next pericentre passage at $t = 7200$. With each passage through the envelope of the first merger product, the orbit of the third star decays and more mass is ejected until ultimately, at $t = 8000$, the three-body merger product is formed.

In cases 250 and 261, the impact of the relatively low-mass intruder into the primary causes the outer layers of the latter to expand and overflow its Roche lobe, resulting ultimately in a stable binary. Fig. 18 shows masses and separations of stars for case 261, which begins with the three stars in a resonant interaction. At $t = 83$, the lowest mass star is absorbed into the largest star. The collision immediately ejects $1 M_{\odot}$ of material and leaves the two remaining stars in an eccentric binary ($e \approx 0.4$). A fraction of a solar mass is also placed into a circumbinary envelope: this fluid is not gravitationally bound to either star individually but rather to the remaining binary as a whole. As the binary grinds through the envelope, the orbit gradually circularizes, as can be seen by examining the separation curve in the bottom frame of Fig. 18. By $t \approx 6 \times 10^4$, the envelope has been effectively removed and the binary has essentially reached a steady state with an orbital period of 113 time units (50 h) and a separation of $26 R_{\odot}$. The calculation for this case lasted more than 3.3×10^6 iterations and covered a timespan of over 80 000 time units (over 4 yr simulation time). During this calculation, total energy and angular momentum were conserved to better than 0.1 per cent.

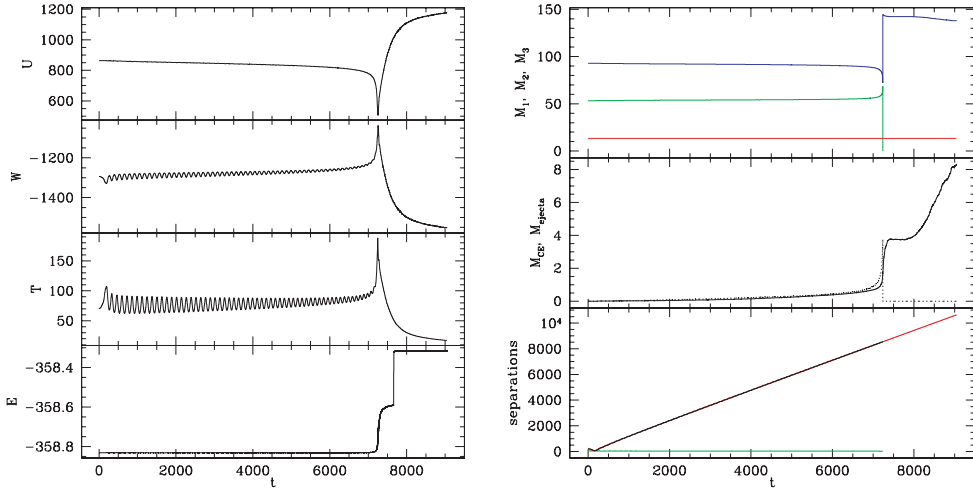


Figure 12. In the left-hand panel, we show the time evolution of internal energy U , gravitational potential energy W , kinetic energy T and total energy E for case 260. In the right-hand panel, we display the evolution of stellar masses and separations: the top frame shows the masses of components 1, 2 and 3, represented by blue, green and red curves, respectively; the middle frame plots the amount of mass ejected (solid curve) and bound in a circumbinary envelope (dotted curve); and the bottom frame shows the separations between components 1 and 2 (green), between 1 and 3 (red), and between 2 and 3 (black).

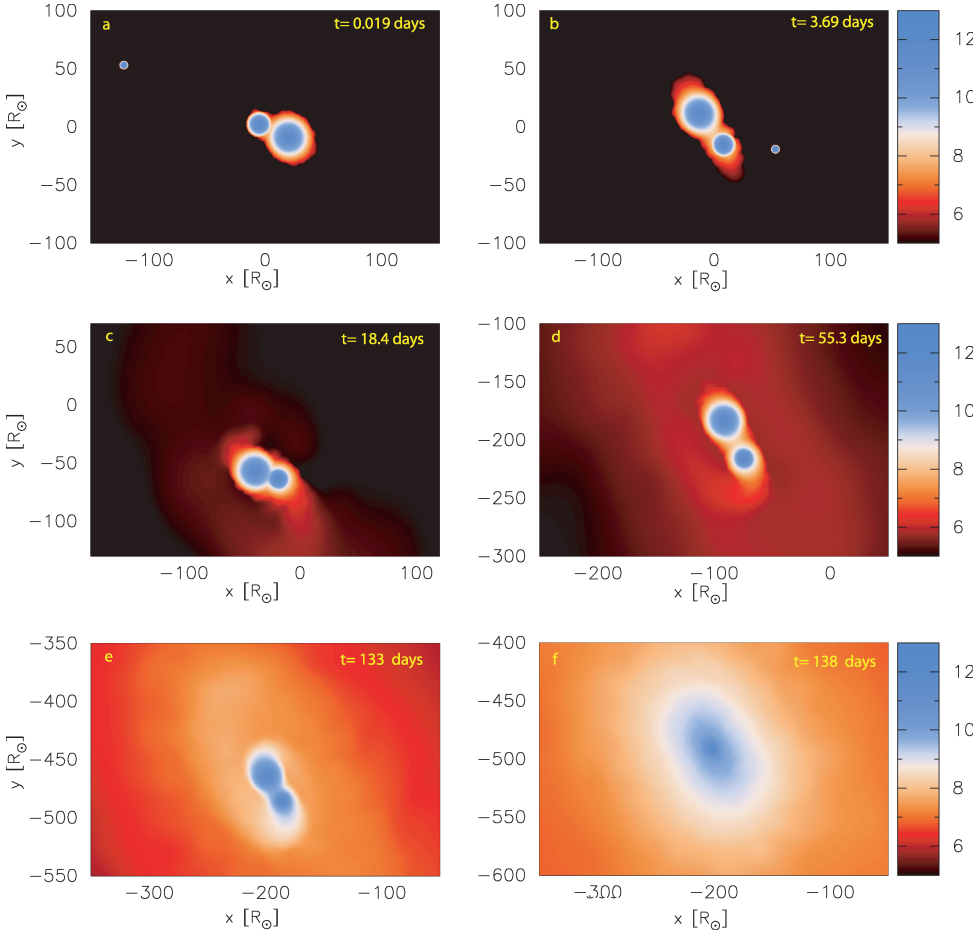


Figure 13. Column density along lines of sight perpendicular to the xy plane at various times for the same hydrodynamic calculation of case 260. As in previous figures, colours represent column density in units of g cm^{-2} on a logscale.

5.2 The effect of numerical resolution

Because of the longevity of three-body interactions, most of our simulations are limited to $N \approx (1\text{--}2) \times 10^4$ particles. Even with

this relatively low number of particles, a single simulation may take a few weeks to complete, as it typically needs to span at least several thousand time units. To test whether our results are affected by numerical artefacts, we recalculated a few of the simulations in

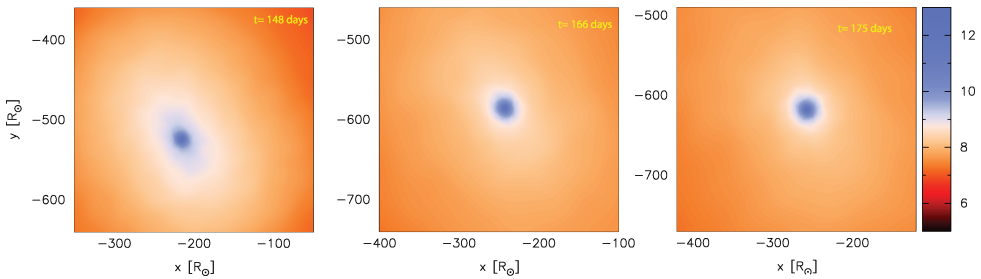


Figure 14. Column density along lines of sight perpendicular to the xy plane at various times for the same hydrodynamic calculation of case 260. While the inner regions of the product become more compact and spherically symmetric, the outer regions increase in size and maintain an elongated shape. As in previous figures, colours represent column density in units of g cm^{-2} on a logscale.

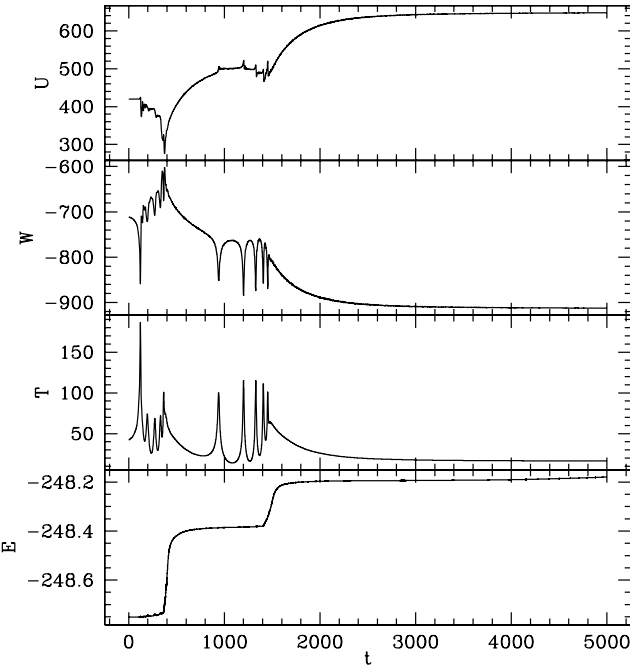


Figure 15. Internal energy U , gravitational energy W , kinetic energy T and total energy E versus time for case 298. Peaks in T and associated dips in W correspond to close passes or mergers between the stars. Note that the total energy is conserved to about 0.2 per cent over the interval shown.

high resolution. In most cases, the results are only weakly dependent on the resolution. In particular, a case of interest is case 204, which begins with three single stars in the middle of the resonance interaction. In Fig. 19, we present the time evolution of the energy for two resolutions. One may see from the kinetic energy plot that the first close interaction occurs at $t \simeq 75$. The further behaviour of the three stars bear characteristics of typical resonant interactions, with kinetic and gravitational potential energy exhibiting aperiodic oscillations of different magnitudes until $t \simeq 200$. At this time two of the three stars merge, and the remaining binary gradually decays. In the high resolution case (right-hand panel in Fig. 19), the initial merger occurs somewhat earlier than in the low-resolution case. Because this kind of interaction is chaotic, it is well known that the details at the level of trajectories are resolution sensitive (Davies et al. 1993b; Freitag & Benz 2005). However, the final outcome is consistent between the two resolutions: all three stars eventually merge (Table 3). Moreover, the mass and energy of the ejecta, as well as the kick velocity of the merger product, change by at most a

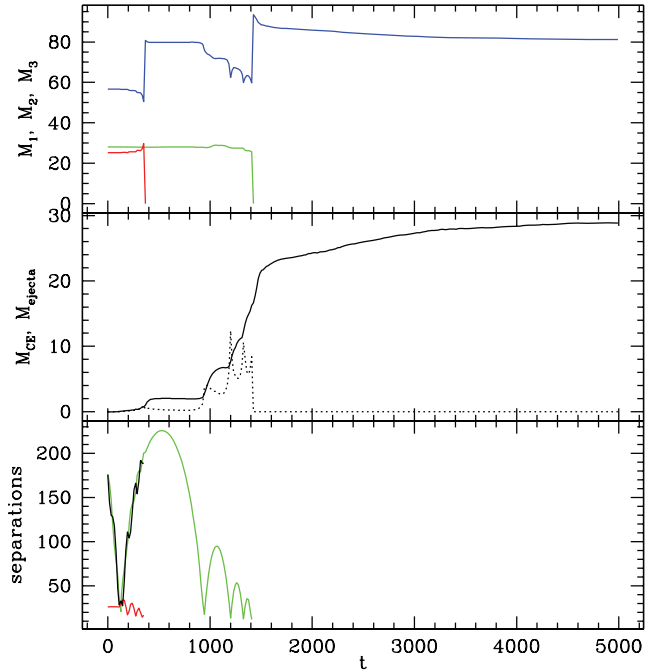


Figure 16. Masses and separations versus time for the calculation displayed in Fig. 15, case 298. The top frame shows the masses of components 1, 2 and 3, represented by blue, green and red curves, respectively. The middle frame plots the amount of mass ejected (solid curve) and bound in a circumbinary envelope (dotted curve). The bottom curves show the separations between components 1 and 2 (green), between 1 and 3 (red), and between 2 and 3 (black).

factor of 2. In Fig. 20, we show the time evolution of masses of three stars, the mass of ejected fluid and the separation between stars.

Another interesting case is 299, in which a massive binary ($52.3 + 16.9 M_{\odot}$) is intruded upon by a massive star ($52.3 M_{\odot}$). In Figs 21 and 22, we show the time evolution of energies and global quantities, such as the masses of stars, the ejecta mass, and the stellar separations. Even though there are some differences, the general agreement between these two simulations is excellent. The merger between two of the three stars (the intruder and the primary of the binary) occurs at $t \simeq 110$, and further binary decay lasts for more than 1200 units. Mass loss and energy of ejected fluid are consistent between these two runs of different resolution.

In Fig. 23, we examine the effects of resolution for four separate simulations of case 202 with the number of particles varying by a factor of 15 from the lowest resolution treatment to the highest resolution. The agreement is excellent, with even the lowest resolution

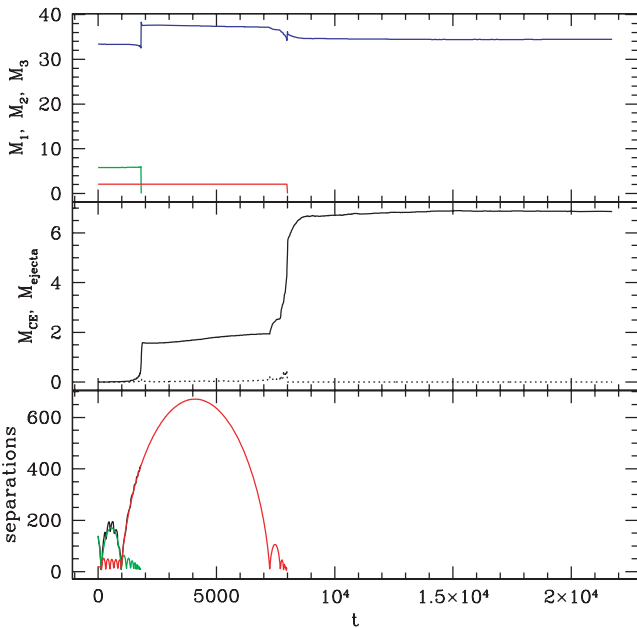


Figure 17. Like Fig. 16, but for case 256.

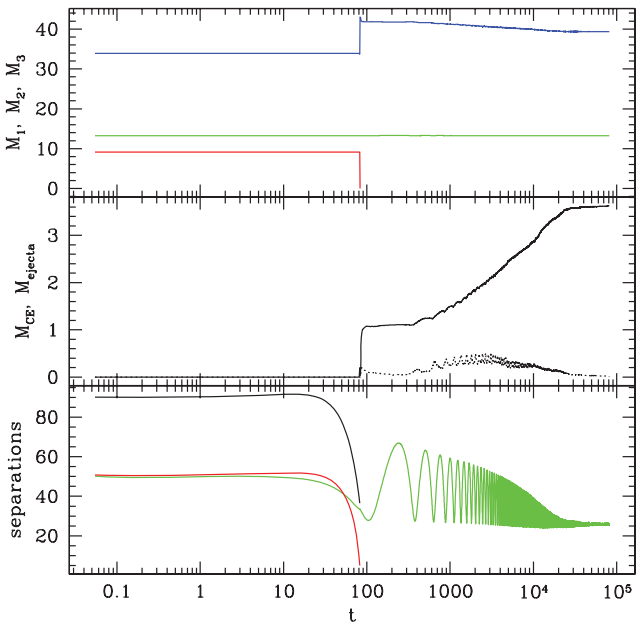


Figure 18. Like Figs 16 and 17, but for case 261, and with time plotted on a logarithmic scale so that the long-term evolution and circularization of the resulting binary can be more easily observed.

simulation capturing all important aspects of the orbital dynamics. The small bump in the kinetic energy T shortly after the time $t = 100$ corresponds to the absorption of the $0.120 M_{\odot}$ star into the $57.9 M_{\odot}$ star, which excites oscillations in the merger product that are visible in the internal energy U and gravitational potential energy W curves. The merger product is left orbiting the $29.9 M_{\odot}$ star in a stable binary with eccentricity $e = 0.583$ and semimajor axis $a = 127 R_{\odot}$: the peaks in T and simultaneous dips in W correspond to the periastron passages.

In Fig. 24, we show the projected trajectories of the three stars in case 246 of masses 42.2 , 38.3 and $1.37 M_{\odot}$, as calculated with a point-mass integrator (top left frame), by using sticky spheres

(top right frame) and with the hydrodynamics code (bottom four frames) with different resolution. In all cases, the $1.37 M_{\odot}$ intruder approaches the circular binary on a hyperbolic trajectory with eccentricity $e = 1.09$. In the point-mass approximation, the intruder reaches a minimum separation of $4.90 R_{\odot}$ from the secondary and then slingshots back outwards on a trajectory with eccentricity $e = 1.05$. The interaction increases the semimajor axis of the binary slightly to $28.5 R_{\odot}$, while also perturbing its eccentricity to $e = 0.0424$. In the sticky sphere approximation, a merger between the intruder and the secondary of the binary occurs during the initial pericentre passage, followed shortly thereafter by a second merger with the primary.

The case plays out qualitatively differently when the hydrodynamics is followed. The intruder again passes to a minimum separation of about $5 R_{\odot}$ from the core of the secondary, well within its $11 R_{\odot}$ stellar radius, and then begins to retreat. The impact, however, transfers energy into oscillations of the secondary and the intruder is not moving fast enough to escape further than about $40 R_{\odot}$ from the secondary. The hydrodynamic calculations indicate that the intruder makes a second pericentre passage through the secondary, but these calculations deviate depending on the resolution: the resulting trajectories do not converge as the number of particles is increased up to $N = 84642$ due to the chaotic nature of the orbits.

In the case of our relatively low-resolution $N = 10554$ calculation of case 246, the intruder is shot out to a distance of over $100 R_{\odot}$. Finally, the intruder makes one final pass through the secondary, and is ejected out of the system on a trajectory with $e = 1.3$. The removal of orbital energy from the binary initiates a mass transfer instability. The primary cannibalizes the secondary and, as the binary merges, $0.06 M_{\odot}$ of material is ejected. At this time, the blue and green curves in Fig. 24 merge into a single blue curve (see the lower right hand corner of the middle left frame). Masses and orbital parameters for this calculation are shown in Fig. 25.

The $N = 21204$ and 42294 calculations of case 246 yield qualitatively similar results. After the third pericentre passage of the intruder through the secondary, the two stars merge. The resulting binary, surrounded by an envelope of gas removed from the secondary by the impacts, ultimately merges. In our highest resolution calculation of this case ($N = 84642$), the intruder does not immediately merge with either star in the binary, but rather the three stars move around one another in a long-lived resonance interaction before ultimately all three stars merge.

6 DISCUSSION AND CONCLUSIONS

We present a set of hydrodynamical simulations of 40 encounters between three stars. The initial conditions are taken from the high-precision direct N -body simulations of Gaburov et al. (2008a), who studied the onset of collision runaway in young star clusters. Most of the collisions (31) involve a massive binary star intruded upon by, generally, a lower mass star. The rest of the collisions (9) occur between three single stars which are in the middle of the resonant interaction. All the simulations were carried out with both the SPH method and in the sticky sphere approximation.

If only initial and final states are of interest, the sticky sphere method provides the appropriate outcome of the encounter in about three out of every four cases. In the cases where sticky spheres result in a merger between three stars, our hydrodynamic simulations tend to give a similar result. However, if one is interested in mass loss, close inspection reveals that a considerable amount of mass can be ejected in double mergers. In addition, the collision product acquires a kick velocity, which is usually a result of the asymmetric

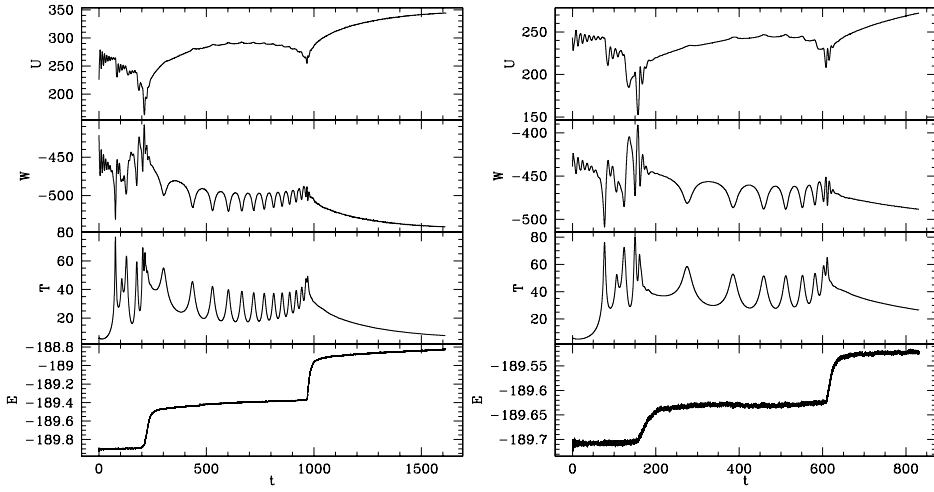


Figure 19. Internal energy U , gravitational potential energy W , kinetic energy T and total energy E versus time t for two simulations of case 204 that differ in resolution: $N = 11946$ (left-hand panel) and 60024 (right-hand panel).

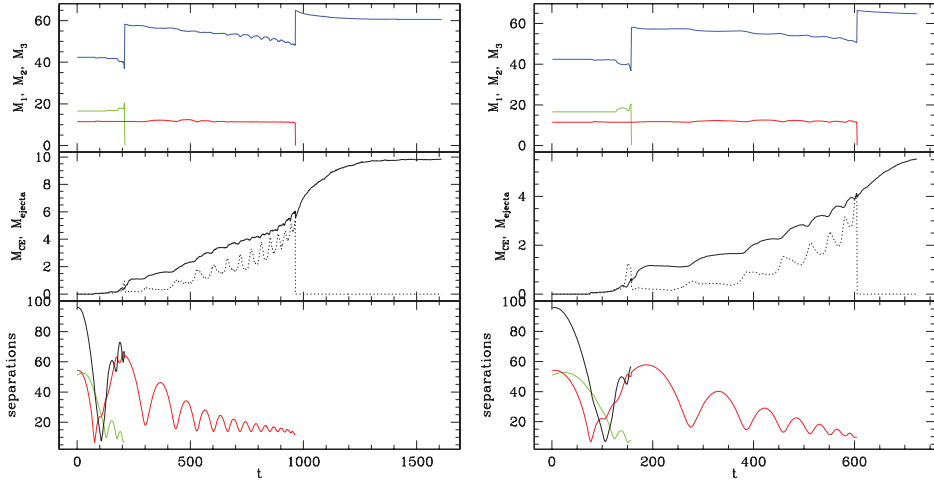


Figure 20. Masses and separations versus time for two simulations of case 204: $N = 11946$ (left-hand panel) and 60024 (right-hand panel). The top frame shows the masses of components 1, 2 and 3, represented by blue, green and red curves, respectively. The middle frame plots the amount of mass ejected (solid curve) and bound in a circumbinary envelope (dotted curve). The bottom curves show the separations between components 1 and 2 (green), between 1 and 3 (red), and between 2 and 3 (black).

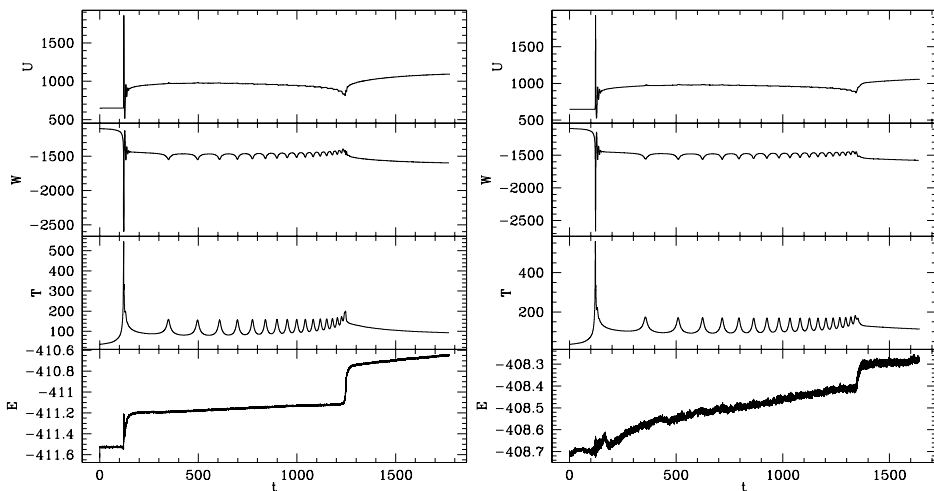


Figure 21. Internal energy U , gravitational potential energy W , kinetic energy T and total energy E versus time t for two simulations of case 299 that differ in resolution: $N = 10194$ (left-hand panel) and 102540 (right-hand panel).

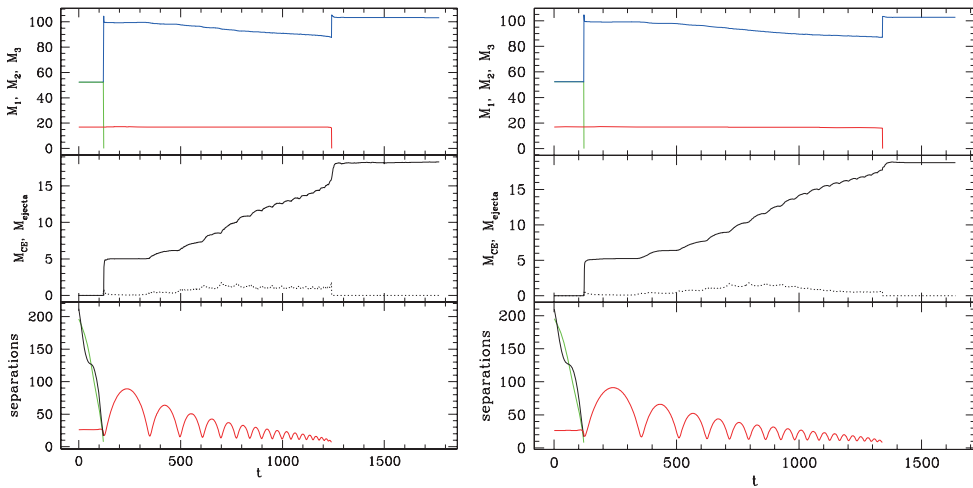


Figure 22. Masses and separations versus time for two simulations of case 299: $N = 10194$ (left-hand panel) and 102540 (right-hand panel). Line types are as in Fig. 20.

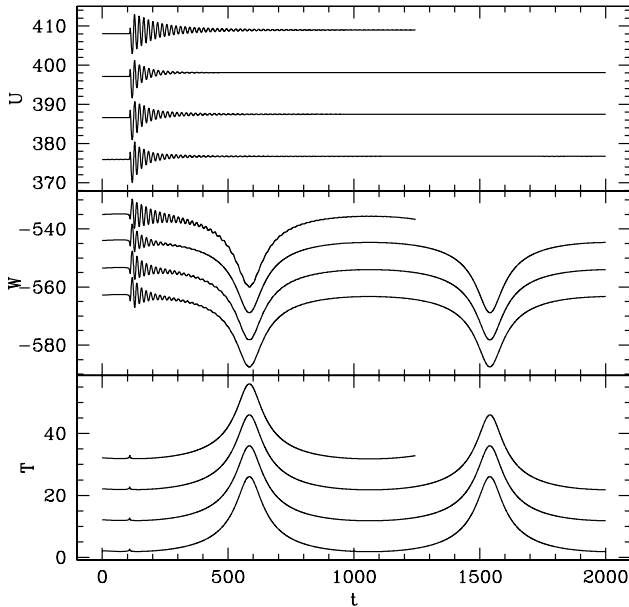


Figure 23. Internal energy U , gravitational potential energy W and kinetic energy T versus time t for four simulations of case 202 that differ in resolution: $N = 6138$ (bottom curve), 11466 (second from bottom), 22380 (third from bottom), 91956 (top). The energy scale on the left axis corresponds to the low resolution $N = 6138$ case: the other energy curves have been offset by 10, 20 and 30 energy units to facilitate the comparison.

mass ejection. The kick velocity can be sufficiently high to eject the merger product to the cluster halo and even to escape. In cases where only two stars merge and the third escapes, the kick velocity is large enough that the collision product could be ejected out of the star cluster completely. Therefore, it is not completely unreasonable to expect collision products to be observed in the outer regions of young star cluster, and the Pistol star in the Quintuplet cluster (Figer et al. 1998) may well be a merger product resulting from an encounter between a single and a binary star.

The sticky sphere approximation, however, fails in several cases. On occasion, this approximation predicts the formation of a binary with a merger product as one of the components (cases 214, 253, 260 and 262), an interesting outcome from either an observational or

theoretical point of view. Detailed hydrodynamic modelling of the same cases, however, show that a complete merger is a more likely outcome, if the interaction is mild; otherwise, the outcome is two unbound stars. In another case, the sticky sphere method predicts either one (case 207) or two collisions (case 222) in a system, but the hydrodynamic simulations predict a fly-by. These are the cases for grazing encounters which result in the ejection of the intruder star. If the semimajor axis of the binary is sufficiently large, binaries tend to avoid mergers and become eccentric instead.

For those situations in which the sticky sphere algorithm predicts a single merger event, the result is incorrect in almost half of the situations. It is important to keep in mind that the condition for a merger in the sticky sphere approximation is energy independent, and therefore if two stars with large enough velocities have a grazing collision, this method will incorrectly predict a complete merger.

Thus, in an environment with high-velocity dispersion, such as galactic nuclei in which the velocity dispersion is typically at least an order of magnitude larger than in the cores of young massive star clusters, the sticky sphere approximation may fail more often. In such environments, the merger cross-section is reduced, as grazing interactions between stars may not necessarily lead to mergers (Freitag & Benz 2005). While this could be improved by a more sophisticated effective radius of the merger product (we use simply $R_1 + R_2$), it is unlikely that simple recipes can correctly reproduce the richness of the hydrodynamic results, especially if one is interested in the close interaction between three or more stars.

All of our collision products possess some amount of angular momentum. In some cases, the angular momentum is large enough that the shape of the collision product substantially deviates from spherical symmetry. Evolving such an object is a challenge for stellar evolution codes, given that even the evolution of non-rotating massive collision product is a formidable task (Glebbeek 2008). In addition, there still exist problems on even hydrodynamical grounds, as some of our rotating collision products are gradually losing mass even at the termination of our hydrodynamic calculations. The reason for this mass loss is due to spurious transport of angular momentum outwards caused by artificial viscosity (Lombardi et al. 1999), as described in Section 5. The precise time-scale of this effect depends on numerical parameters and the treatment of artificial viscosity. For example, in case 220, the progression of the stellar collisions is essentially the same in the $N = 20178$ and $N = 46296$

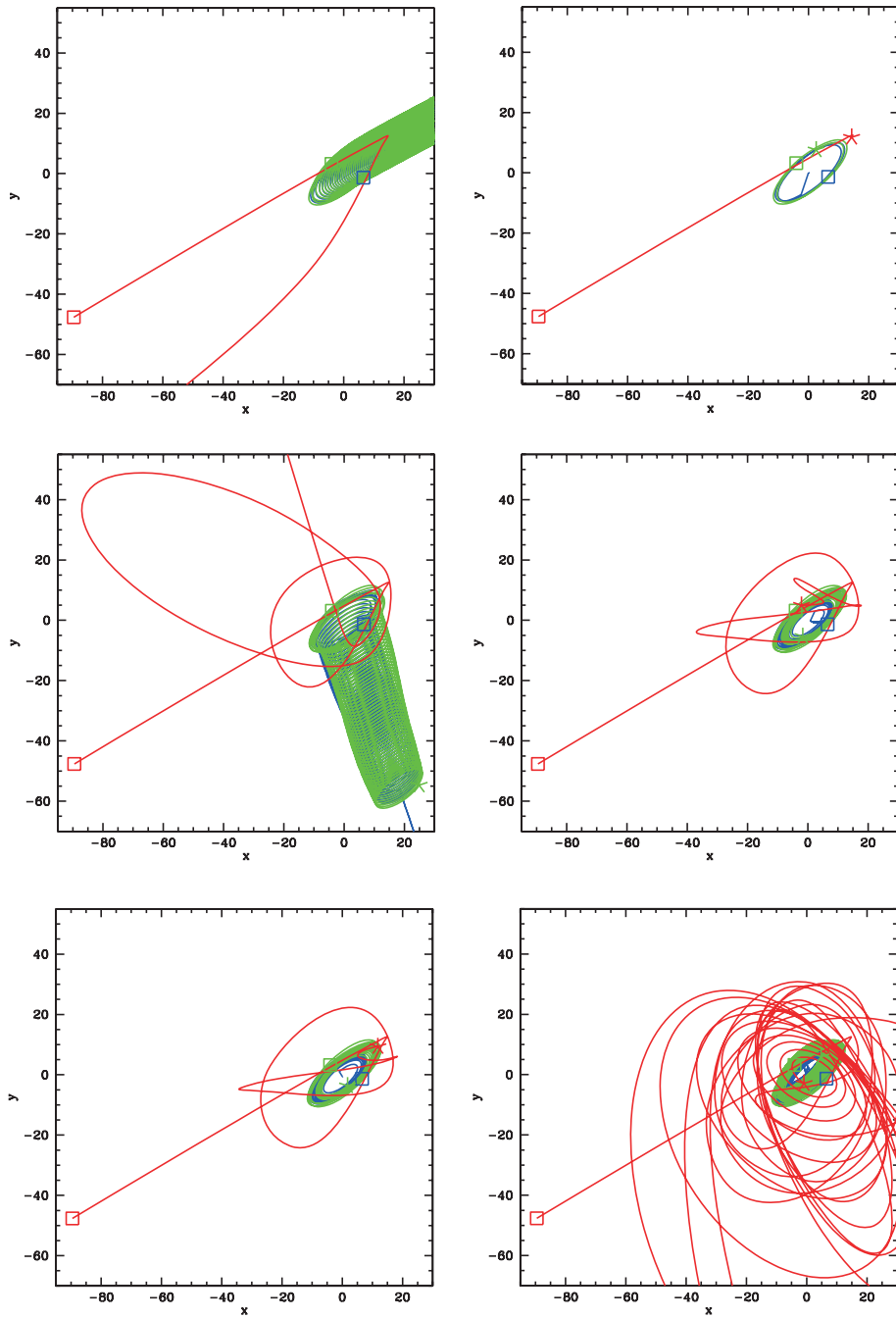


Figure 24. Trajectories projected on to the xy plane for case 246 as calculated in a pure point-mass approximation (top left), in a sticky sphere approximation (top right), by our hydrodynamics code with $N = 10\,554$ (middle left), with $N = 21\,204$ (middle right), with $N = 42\,294$ (bottom left) and with $N = 84\,642$ (bottom right). We adopt the convention that the trajectory of the most massive star is represented by the blue curve, the intermediate mass star by the green curve, and the lowest mass star by the red curve. The initial conditions are marked by squares, while the final position of an object before it merges with another one is marked by a 5-point asterisk.

calculations. In the higher resolution simulation, however, the angular momentum transport and resulting mass loss in the final collision product progresses more slowly. It is worth noting, however, that *physical* angular momentum transport mechanisms, such as stellar winds and magnetic braking, would have a similar qualitative effect but on a longer time-scale (Sills et al. 2005).

Stellar collisions in a young dense star cluster are expected to occur in the first few million years of the cluster lifetime (Portegies Zwart et al. 1999). At this age, the star cluster may still be embedded

in natal gas (Lada & Lada 2003), and therefore if the ejecta is energetic enough the state of the gas may be considerably disturbed. Such a mechanism has recently been proposed within the context of globular clusters (Umbreit, Chatterjee & Rasio 2008). In the case of young star clusters, our results suggest that the ejecta emanating from stellar collisions is energetic enough to significantly disturb and even eject the remaining gas. Indeed, a young massive star cluster with a star formation efficiency of about 50 per cent has about $10^{49}\text{--}10^{50}$ ergs in binding energy of the remaining gas. Our

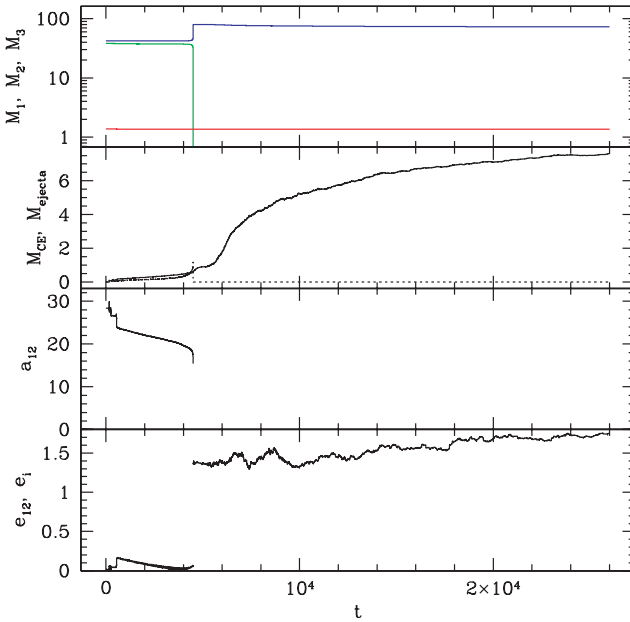


Figure 25. Evolution versus time of, from the top of the figure to the bottom, the stellar masses, mass in a circumbinary envelope (dotted curve) as well as in ejecta (solid curve), semimajor axis a_{12} of the binary, and eccentricity e_{12} of the binary ($t < 4500$) as well as eccentricity e_i of the third star as it departs from the merger product ($t > 4500$) for the $N = 10\,554$ SPH calculation of case 246.

results show that the energy of the ejected fluid in stellar collisions exceeds 10^{49} ergs, and in two cases (cases 220 and 299) even 10^{50} ergs. Since collisions are expected to occur in the core of a star cluster, it would be just a matter of a few collisions to significantly perturb or largely expel the natal gas from the central region. In the case of a runaway merger (Portegies Zwart et al. 2004; Freitag et al. 2006), we therefore expect that the gas will be expelled from the central regions before the end of runaway.

ACKNOWLEDGMENTS

JCL thanks Alex Brown for useful conversations. We acknowledge the use of the three-dimensional virtual collaboration environment QWAQ FORUMS, which greatly facilitated the remote collaboration leading to this paper. We thank the anonymous referee for the valuable comments that helped to improve the manuscript. This work was supported by the Netherlands Research School for Astronomy (NOVA), the National Science Foundation under Grant No. 0703545 No. PHY05-51164 and by NWO (grants #635.000.303 and #643.200.503, VIDI grant #639.042.607 and VICI grant #6939.073.803). Column density plots in this paper were produced using SPLASH, a publicly available visualization tool for SPH (Price 2007). This work used the MUSE framework, which is available at <http://muse.li>.

REFERENCES

- Adams T., Davies M. B., Sills A., 2004, MNRAS, 348, 469
 Balsara D. S., 1995, J. Computational Phys., 121, 357
 Baumgardt H., Kroupa P., 2007, MNRAS, 380, 1589
 Belleman R. G., Bédorf J., Portegies Zwart S. F., 2008, New Astron., 13, 103
 Benz W., Hills J. G., 1987, ApJ, 323, 614
 Cleary P. W., Monaghan J. J., 1990, ApJ, 349, 150
 Cohn H., Hut P., Wise M., 1989, ApJ, 342, 814
 Dale J. E., Davies M. B., 2006, MNRAS, 366, 1424
 Davies M. B., Benz W., Hills J. G., 1993a, ApJ, 411, 285
 Davies M. B., Ruffert M., Benz W., Muller E., 1993b, A&A, 272, 430
 Davies M. B., Benz W., Hills J. G., 1994, ApJ, 424, 870
 Davies M. B., Blackwell R., Bailey V. C., Sigurdsson S., 1998, MNRAS, 301, 745
 Eggleton P. P., 1971, MNRAS, 151, 351
 Figer D. F., Najjar F., Morris M., McLean I. S., Geballe T. R., Ghez A. M., Langer N., 1998, ApJ, 506, 384
 Fregeau J. M., Gürkan M. A., Joshi K. J., Rasio F. A., 2003, ApJ, 593, 772
 Fregeau J. M., Cheung P., Portegies Zwart S. F., Rasio F. A., 2004, MNRAS, 352, 1
 Freitag M., Benz W., 2005, MNRAS, 358, 1133
 Freitag M., Gürkan M. A., Rasio F. A., 2006, MNRAS, 368, 141
 Fukushige T., Taiji M., Makino J., Ebisuzaki T., Sugimoto D., 1996, ApJ, 468, 51
 Gaburov E., Gualandris A., Portegies Zwart S., 2008a, MNRAS, 384, 376
 Gaburov E., Lombardi J. C., Portegies Zwart S., 2008b, MNRAS, 383, L5
 Gaburov E., Harfst S., Portegies Zwart S., 2009, preprint (arXiv:0902.4463)
 Glebbeek E., 2008, PhD thesis, Utrecht University
 Glebbeek E., Pols O. R., 2008, A&A, 488, 1017
 Glebbeek E., Pols O. R., Hurley J. R., 2008, A&A, 488, 1007
 Glebbeek E., Gaburov E., de Mink S. E., Pols O. R., Portegies Zwart S. F., 2009, A&A, 497, 255
 Gürkan M. A., Fregeau J. M., Rasio F. A., 2006, ApJ, 640, L39
 Hamada T., Iitaka T., 2007, preprint (astro-ph/0703100)
 Harrington R. S., 1970, AJ, 75, 1140
 Heggie D. C., 1975, MNRAS, 173, 729
 Heggie D. C., Hut P., 1993, ApJS, 85, 347
 Heggie D. C., Trenti M., Hut P., 2006, MNRAS, 368, 677
 Hills J. G., 1992, AJ, 103, 1955
 Hut P., 1983, ApJ, 268, 342
 Hut P., Bahcall J. N., 1983, ApJ, 268, 319
 Lada C. J., Lada E. A., 2003, ARA&A, 41, 57
 Lombardi J. C., Jr, Rasio F. A., Shapiro S. L., 1995, ApJ, 445, L117
 Lombardi J. C., Sills A., Rasio F. A., Shapiro S. L., 1999, J. Computational Phys., 152, 687
 Lombardi J. C., Jr, Warren J. S., Rasio F. A., Sills A., Warren A. R., 2002, ApJ, 568, 939
 Lombardi J. C., Thrall A. P., Deneva J. S., Fleming S. W., Grabowski P. E., 2003, MNRAS, 345, 762
 Lombardi J. C., Jr, Proulx Z. F., Dooley K. L., Theriault E. M., Ivanova N., Rasio F. A., 2006, ApJ, 640, 441
 McMillan S. L. W., 1986, ApJ, 306, 552
 Monaghan J. J., 1992, ARA&A, 30, 543
 Monaghan J. J., 1997, J. Computational Phys., 136, 298
 Monaghan J. J., 2002, MNRAS, 335, 843
 Monaghan J. J., Lattanzio J. C., 1985, A&A, 149, 135
 Portegies Zwart S. F., Makino J., McMillan S. L. W., Hut P., 1999, A&A, 348, 117
 Portegies Zwart S. F., McMillan S. L. W., 2002, ApJ, 576, 899
 Portegies Zwart S. F., Baumgardt H., Hut P., Makino J., McMillan S. L. W., 2004, Nat, 428, 724
 Portegies Zwart S. F., Belleman R. G., Geldof P. M., 2007a, New Astron., 12, 641
 Portegies Zwart S., Gaburov E., Chen H.-C., Gürkan M. A., 2007b, MNRAS, 378, L29
 Portegies Zwart S., McMillan S., Harfst S. E. A., 2009, New Astron., 14, 369
 Price D. J., 2007, Publ. Astron. Soc. Aust., 24, 159
 Price D. J., Monaghan J. J., 2007, MNRAS, 374, 1347
 Rasio F. A., Lombardi J. C., Jr, 1999, J. Comput. Appl. Math., 109, 213
 Rasio F. A., Shapiro S. L., 1994, ApJ, 432, 242
 Rosswog S., 2009, preprint (arXiv:0903.5075)
 Sills A., Faber J. A., Lombardi J. C., Jr, Rasio F. A., Warren A. R., 2001, ApJ, 548, 323
 Sills A., Adams T., Davies M. B., 2005, MNRAS, 358, 716

- Sills A., Karakas A., Lattanzio J., 2009, ApJ, 692, 1411
 Springel V., 2005, MNRAS, 364, 1105
 Springel V., Hernquist L., 2002, MNRAS, 333, 649
 Sugimoto D., Bettwieser E., 1983, MNRAS, 204, 19P
 Suzuki T. K., Nakasato N., Baumgardt H., Ibukiyama A., Makino J., Ebisuzaki T., 2007, ApJ, 668, 435
 Umbreit S., Chatterjee S., Rasio F. A., 2008, ApJ, 680, L113

APPENDIX A: DERIVATION OF SPH EQUATIONS OF MOTION

The use of non-equal mass particles in the simulations allows us to resolve both the core and the envelope of parent stars. However, during the merger process, particles of significantly different mass from two or more parent stars mix, and the standard constraint between density and the smoothing length, $h_i = f(\rho_i, C_i)$, becomes inappropriate. Such a constraint naturally involves a constant with dimensionality of mass, C_i . This constant is usually determined during the setup of the initial conditions and therefore reflects the initial mass resolution of particle i , that is the initial total mass of the neighbours of that particle. However, as the particle migrates from one region to another, the mass resolution of the particle should adapt to its new environment. If this does not happen, the particle may have too few or too many neighbours, depending on whether it migrates into a region with, respectively, an average particle mass significantly larger or smaller than in its initial environment. To mend this, we present a new approach that keeps the number of neighbours roughly constant. Here, we can draw an analogy with finite-difference hydrodynamics, either on fixed or moving meshes: the number of neighbouring cells that a given grid cell interacts with is also roughly constant (exactly constant on a fixed mesh) and is, to some degree, independent of the local fluid conditions.

We propose a continuous constraint between an estimate of the number of neighbours and the smoothing length. Relaxing the condition that the neighbour number estimate be an integer, we weight each neighbour with a function that depends on its distance from the particle, $G(r_{ij}/h_i)$, where r_{ij} is separation between the particle i and the neighbour j . Using such a weight function, we estimate the number of neighbours of a given particle i as

$$N_i = \sum_j G(|\mathbf{r}_i - \mathbf{r}_j|, h_i) \equiv \sum_j G_{ij}(h_i). \quad (\text{A1})$$

We find empirically that the following function provides satisfactory results:

$$G(x, h) \equiv V(4h - 4|x - h|, h), \quad (\text{A2})$$

where $0 \leq x < 2h$, otherwise it is equal to zero, and

$$V(x, h) \equiv 4\pi \int_0^x x^2 W(x, h) dx. \quad (\text{A3})$$

Here, $W(x, h)$ is an SPH smoothing kernel with a compact support of $2h$. We use the kernel of Monaghan & Lattanzio (1985), for which the weighting function G takes on the form shown in Fig. A1. Setting N_i to be constant, equation (A1) provides the particle with a necessary constraint between h_i and its estimated instantaneous number of neighbours in a continuous way. In the calculations presented in this paper, we choose $N_i = 22$, which typically results in about 35 to 40 actual neighbours enclosed by the smoothing kernel if the particle distribution is regular. (It is not surprising that the actual number of neighbours is consistently larger than the chosen N_i , as can be seen by noting from Fig. A1 that $G \leq 1$.)

Our choice of roughly 30 to 40 initial neighbours for regular particle distribution is motivated by the analogy with finite difference

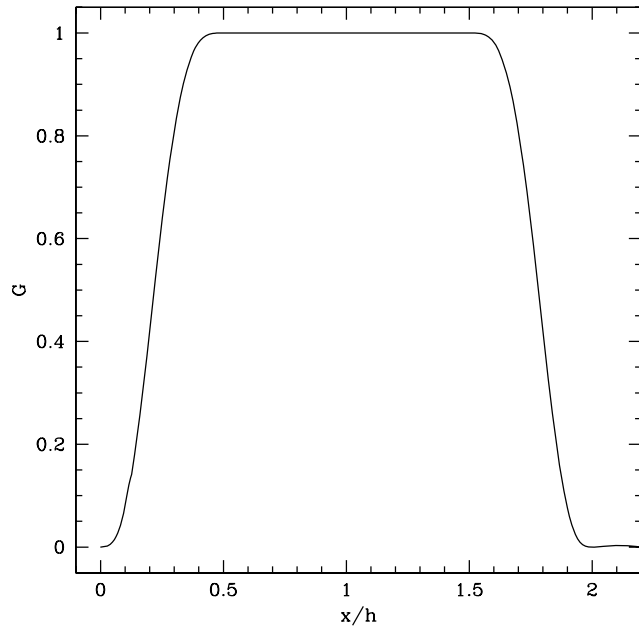


Figure A1. Plotted here versus normalized separation x/h , the weighting function G used to help keep neighbour numbers roughly constant even when non-equal mass particles are used.

schemes. In one dimension, the number of neighbouring cells that are involved in an interaction with a given grid cell depends on the order of the numerical scheme, and is usually two for the second order scheme. Along the same lines, in the variational formulation of SPH, two to four neighbouring particles are usually used in one-dimensional simulations. If we scale this to three dimensions and take into account that a kernel is of a spherical shape, the estimated number of neighbours in three dimensions lies between 20 and 50 for an ordered distribution of particles. The actual number of neighbours in the course of simulations is set by local conditions via equation (A1) and can well exceed the initial number of neighbours, if particles become disordered.

Because our constraint allows particles' smoothing lengths to be a function of particle coordinates, the variational formulation of SPH can be used to derive equations of motion (Monaghan 2002; Springel & Hernquist 2002; Price & Monaghan 2007). In particular, we consider the SPH Lagrangian:

$$\mathcal{L} = \frac{1}{2} \sum_j m_j v_j^2 - \sum_j m_j u_j - \frac{1}{2} \sum_j m_j \phi_j. \quad (\text{A4})$$

Here, m_j is the mass of SPH particle j , v_j and u_j its velocity and specific internal energy, respectively, and ϕ_j is its gravitational potential, which is defined as

$$\phi_j = \sum_k m_k g(|\mathbf{r}_j - \mathbf{r}_k|, h_j) \equiv \sum_k m_k g_{jk}(h_j), \quad (\text{A5})$$

where $g(x, h)$ is the gravitational potential between two SPH particles of unit mass. The Euler–Lagrange equations resulting from this Lagrangian are

$$m_i \dot{\mathbf{v}}_i = - \sum_j m_j \left(\frac{\partial u}{\partial \rho} \right)_{s,j} \frac{d\rho_j}{d\mathbf{r}_i} - \frac{1}{2} \sum_j m_j \frac{d\phi_j}{d\mathbf{r}_i}. \quad (\text{A6})$$

Here, the first term is the hydrodynamic force, $m_i \mathbf{a}_{h,i}$, the second term is the gravitational force, $m_i \mathbf{a}_{g,i}$, and the partial derivative, $(\partial u / \partial \rho)_s$, is evaluated at constant entropy s . Using the SPH

definition of density,

$$\rho_j = \sum_k m_k W(|\mathbf{r}_j - \mathbf{r}_k|, h_j) \equiv \sum_k m_k W_{jk}(h_j), \quad (\text{A7})$$

we derive its gradient

$$\frac{d\rho_j}{d\mathbf{r}_i} = \sum_k m_k \nabla_i W_{ik}(h_i) \delta_{ij} + m_i \nabla_i W_{ij}(h_j) + \sum_k m_k \frac{\partial W_{jk}(h_j)}{\partial h_j} \frac{dh_j}{d\mathbf{r}_i}. \quad (\text{A8})$$

Differentiating equation (A1) with respect to \mathbf{r}_i , we find

$$\chi_j \frac{dh_j}{d\mathbf{r}_i} = - \sum_k \nabla_i G_{jk}(h_i) \delta_{ij} - \nabla_i G_{ij}(h_j), \quad (\text{A9})$$

where

$$\chi_j \equiv \sum_k \frac{\partial G_{jk}(h_j)}{\partial h_j}. \quad (\text{A10})$$

With these equations, it is straightforward to derive accelerations due to pressure

$$\mathbf{a}_{h,i} = - \sum_j m_j \frac{P_i}{\rho_i^2} \left[\nabla_i W_{ij}(h_i) - \frac{\omega_i}{\chi_i m_j} \nabla_i G_{ij}(h_i) \right] \quad (\text{A11})$$

$$- \sum_j m_j \frac{P_j}{\rho_j^2} \left[\nabla_i W_{ij}(h_j) - \frac{\omega_j}{\chi_j m_i} \nabla_i G_{ij}(h_j) \right], \quad (\text{A12})$$

and due to gravity

$$\mathbf{a}_{g,i} = - \frac{1}{2} \sum_j m_j [\nabla_i g_{ij}(h_i) + \nabla_i g_{ij}(h_j)] \quad (\text{A13})$$

$$+ \frac{1}{2} \sum_j m_j \frac{\Psi_i}{\chi_i m_j} \nabla_i G_{ij}(h_i) \quad (\text{A14})$$

$$+ \frac{1}{2} \sum_j m_j \frac{\Psi_j}{\chi_j m_i} \nabla_i G_{ij}(h_j). \quad (\text{A15})$$

Here, we define two more quantities:

$$\omega_j \equiv \sum_k m_k \frac{\partial W_{jk}(h_j)}{\partial h_j} \quad (\text{A16})$$

and

$$\Psi_i \equiv \sum_k m_k \frac{\partial g_{ik}(h_i)}{\partial h_i}. \quad (\text{A17})$$

Following the approach of Monaghan (2002) (see their Section 2.3), we find the rate of change of the specific internal energy to be

$$\frac{du_i}{dt} = \frac{P_i}{\rho_i^2} \sum_j m_j (\mathbf{v}_i - \mathbf{v}_j) \cdot \left[\nabla_i W_{ij}(h_i) - \frac{\omega_i}{\chi_i m_j} \nabla_i G_{ij}(h_i) \right], \quad (\text{A18})$$

which guarantees conservation of total energy and entropy in the absence of shocks. In order to handle shock waves effectively while maintaining energy conservation, we augment these equations with an artificial viscosity term that is a hybrid between that of Balsara (1995) and Monaghan (1997):

$$\Pi_{ij} = \left(\frac{p_i}{\rho_i^2} + \frac{p_j}{\rho_j^2} \right) (-\alpha \mu_{ij} + \beta \mu_{ij}^2), \quad (\text{A19})$$

with $\alpha = 1$ and $\beta = 2$. In our treatment,

$$\mu_{ij} = \frac{(\mathbf{v}_i - \mathbf{v}_j)(\mathbf{r}_i - \mathbf{r}_j)}{|\mathbf{r}_i - \mathbf{r}_j|} \frac{f_i + f_j}{c_i + c_j} \quad (\text{A20})$$

if $(\mathbf{v}_i - \mathbf{v}_j)(\mathbf{r}_i - \mathbf{r}_j) < 0$; otherwise $\mu_{ij} = 0$. Here, c_i is the sound speed at particle i . See Lombardi et al. (2006) for the definition of the form factor f_i and for additional details on how the artificial viscosity is incorporated.

The evolution equations are integrated using a symplectic integrator with shared symmetrized time-steps, as in Springel (2005). Our shared time-step is determined as

$$\Delta t = \text{Min}_i \left[(\Delta t_{1,i}^{-1} + \Delta t_{2,i}^{-1})^{-1} \right], \quad (\text{A21})$$

where for each SPH particle i , we use

$$\Delta t_{1,i} = C_{N,1} \frac{h_i}{\text{Max} [\text{Max}_j (\kappa_{ij}), \text{Max}_j (\kappa_{ji})]} \quad (\text{A22})$$

with

$$\kappa_{ij} \equiv \left[\left(\frac{p_i}{\rho_i^2} + \frac{1}{2} \Pi_{ij} \right) \rho_i \right]^{1/2}, \quad (\text{A23})$$

and

$$\Delta t_{2,i} = C_{N,2} \frac{u_i}{|du_i/dt|}. \quad (\text{A24})$$

For the simulations presented in this paper, $C_{N,1} = 0.2$ to 0.3 and $C_{N,2} = 0.05$. The Max_j function in equation (A22) refers to the maximum of the value of its expression for all SPH particles j that are neighbours with i . The denominator of equation (A22) is an approximate upper limit to the signal propagation speed near particle i . The incorporation of Δt_2 enables us to treat shocks without drastically decreasing the time-step during intervals in which the flow is subsonic.

APPENDIX B: INITIAL CONDITIONS

In Table B1, we summarize the raw initial conditions of our calculations in order to facilitate comparisons with any future works.

Table B1. The first column gives the case identification number. The second, third and fourth columns give the masses M_1 , M_2 and M_3 of the colliding stars. Columns 5 through 7 and columns 8 through 10 give the position and velocity, respectively, of star 1 in Cartesian coordinates. Likewise, columns 11 through 13 and columns 14 through 16 give the position and velocity of star 2. The position and velocity of star 3 can be determined from the constraints that the centre of mass be at the origin and that the net momentum is zero. All quantities are in solar units.

ID	M_1	M_2	M_3	x_1	y_1	z_1	$v_{x,1}$	$v_{y,1}$	$v_{z,1}$	x_2	y_2	z_2	$v_{x,2}$	$v_{y,2}$	$v_{z,2}$	
201	84.1	27.1	0.250	81.6	33.9	-7.56	-0.00102	0.0690	0.0777	-254.	-108.	22.0	0.00207	-0.206	-0.237	
202	57.9	29.9	0.120	-52.5	13.8	-37.1	0.0150	0.148	-0.0508	102.	-26.4	71.9	-0.0302	-0.289	0.0977	
203	47.1	36.3	1.09	-7.32	8.64	-9.06	0.474	-0.998E-01	-0.469	-10.5	12.3	-0.620	0.121	0.640	0.275	
206	24.6	21.9	20.6	46.8	20.8	-0.850	-0.434E-02	-0.969E-02	-0.412	23.4	52.8	11.0	0.791	-0.688	0.993	
207	42.2	18.2	0.651	9.29	1.86	-1.35	-0.434E-02	-0.969E-02	-0.412	-19.6	-8.11	-0.774	0.293E-02	0.524E-01	-0.303E-01	
208	86.7	0.513	0.161	-1.86	-1.27	0.139	0.382E-02	0.489E-02	0.505E-03	298.	220.	-21.2	-0.524	-0.454	-0.454	
211	61.7	18.4	8.89	-28.1	1.04	13.5	0.384E-01	-0.676E-01	0.288E-01	117.	-5.11	-46.2	-0.553	0.356	0.620	
212	87.6	27.1	22.7	29.8	18.3	-7.61	0.204	0.155E-01	0.212	15.4	6.21	21.9	-1.21	-0.598	-0.737	
213	76.8	13.6	0.227	-2.97	-3.52	-2.06	-0.137	0.199	-0.810E-01	17.9	16.8	11.8	0.769	-1.10	0.458	
214	17.8	16.8	9.49	2.63	13.0	8.76	-0.343	0.322	-0.150	-6.44	-3.78	-2.14	0.264	-0.0197	-0.350	
217	86.4	28.9	0.110	-11.9	4.92	-0.182	-0.0434	-0.0713	0.367	34.8	-15.7	1.25	0.131	0.216	-1.10	
219	36.6	10.7	9.10	15.9	-7.02	-6.37	0.109	0.155	0.0155	-44.7	24.4	27.7	-0.170	0.111	-0.0360	
220	84.3	68.3	32.7	-12.1	-7.97	-41.0	0.569	0.631	0.369	6.17	-43.2	-13.6	-0.605	-0.636	-0.102	
222	22.8	11.1	5.28	-14.1	-3.42	2.74	0.205	-0.245	-0.146	-41.8	0.696	-17.9	-0.209E-01	0.593	0.325	
223	28.6	19.4	4.57	-31.3	-10.8	37.9	0.118	0.198	-0.453	55.2	16.7	-66.3	-0.208	-0.0781	0.500	
224	48.1	22.0	0.200	-5.22	-4.58	2.42	0.328	-0.136	0.427	10.8	9.03	-5.32	-0.712	0.309	-0.937	
227	16.0	5.62	0.174	-17.9	-19.4	12.1	0.0888	0.116	-0.0455	52.3	55.7	-35.0	-0.268	-0.353	0.121	
231	26.1	25.8	0.411	63.5	5.88	-11.6	-0.415	0.0894	0.137	-63.5	-6.03	11.8	0.418	-0.103	-0.141	
232	19.1	12.2	6.99	-58.6	-7.88	26.5	0.359	0.0774	-0.120	60.4	8.80	-24.4	0.0430	-0.215	-0.245	
233	47.6	28.9	2.94	7.42	-88.9	24.3	-0.100	0.302	-0.999E-01	-9.56	134.	-38.0	0.179	0.179	0.213	
236	40.5	31.4	29.3	-36.0	-41.0	10.9	-0.114	0.849	-0.345	-52.5	-54.1	1.16	0.500	-0.563	0.538	
241	41.7	28.1	11.3	26.2	46.6	46.4	-0.228	-0.205	-0.405	-27.0	-53.1	-49.8	0.760E-01	0.104	0.878	
242	41.1	23.5	0.490	-3.06	-2.81	5.16	-0.0758	-0.516	-0.365	7.38	7.01	-10.6	0.124	0.891	0.646	
245	79.1	43.5	16.0	-48.5	-66.2	-40.1	0.191	0.255	0.369	65.5	81.8	59.6	-0.590	-0.277	-0.375	
246	42.2	38.3	1.37	6.56	-1.36	15.6	0.554	0.546	-0.159	-4.02	3.20	-10.3	-0.631	-0.613	0.147	
249	74.7	0.154	0.110	-0.718	0.256	0.0579	0.00154	-0.00229	-0.000616	328.	-120	-66.3	-0.506	0.217	0.183	
250	44.0	31.9	0.550	1.70	-0.0166	15.0	0.0346	-0.617	0.0335	-2.35	-1.72	-20.4	-0.0446	0.850	-0.0481	
253	53.4	8.55	0.583	-0.664	-1.74	1.73	0.176	-0.0823	-0.104	-2.64	14.7	-14.7	-0.111	0.501	0.666	-0.375
256	33.4	5.84	2.11	16.3	-5.81	9.70	-0.0106	0.0614	-0.0617	-101.	37.5	-52.8	0.489	-0.109	0.396	-0.401
257	97.3	24.9	5.18	-6.21	13.7	-3.31	0.166	0.119	0.0784	30.5	-40.7	13.0	-0.710	-0.439	-0.401	
258	90.4	0.929	0.546	-1.35	-1.00	-0.482	0.00898	0.0159	0.000210	116.	103	47.8	-0.603	-0.669	-0.527	
259	55.9	21.7	11.4	13.0	21.9	7.96	0.208	-0.140	-0.465	-4.92	5.50	-2.09	-0.651	-0.117	1.03	
260	92.9	53.3	13.3	20.3	-8.98	28.8	-0.200	0.648	0.229	-4.97	2.34	-5.17	0.192	-0.939	-0.588	-0.562
261	33.9	13.2	9.17	-4.19	3.93	7.70	-0.122	0.00813	-0.131	11.1	-42.0	-5.62	0.180	-0.0511	-0.401	-0.274
262	31.5	29.3	18.4	-37.9	-23.2	-65.6	-0.249	0.0274	0.575	-6.01	-8.40	-8.67	0.343	0.228	-0.274	-0.527
267	28.6	19.1	14.2	-54.5	16.3	-0.486	0.354	0.313	0.450E-01	107.	-25.5	-2.16	-0.261	0.788E-01	-0.146E-01	-0.146E-01
298	56.7	28.1	25.3	28.0	35.2	-9.25	0.220	0.6918	-0.184	-93.3	-91.4	0.736	0.356	0.0203	0.0203	-0.128E-06
299	52.3	52.3	16.9	82.3	-4.64	-2.27	-0.165	-0.155	-0.195	-114.	0.720E-04	0.175E-03	0.628	-0.208E-06	-0.128E-06	-0.128E-06

This paper has been typeset from a **TEX/LaTeX** file prepared by the author.